

MODELING THE VOID H I COLUMN DENSITY SPECTRUM WITH SUB-GALACTIC HALOS

CURTIS V. MANNING

Astronomy Department, University of California, Berkeley, CA 94720

Draft version November 26, 2018

ABSTRACT

The equivalent width distribution function (EWDF) of H I absorbers specific to the void environment has been recently derived (Manning, 2002). The findings revealed void line densities $dN/dz \simeq 500$ at equivalent widths $W \geq 15.8$ mÅ ($N_{HI} \gtrsim 2.6 \times 10^{12}$ cm⁻²). I show that the void absorbers cannot be diffuse (or so-called filamentary) clouds, expanding with the Hubble flow, as suggested by N-body/hydro simulations. Absorbers are here modeled as the baryonic remnants of sub-galactic perturbations that have expanded away from their dark halos in response to reionization at $z \approx 6.5$. A 1-D Lagrangian hydro/gravity code is used to follow the dynamic evolution and ionization structure of the baryonic clouds for a range of halo circular velocities. The simulation products at $z = 0$ can be combined according to various models of the halo velocity distribution function to form a column density spectrum that can be compared with the observed (Manning, 2002). To explain the observations with these models requires a search of parameter space somewhat beyond the envelope of convention. For a given circular velocity, a halo model more massive than the Navarro, Frenk, & White 1996, 1997 (NFW) halo is required to reproduce the observed line density of absorbers. A more massive, non-singular isothermal halo is used with a more favorable outcome. I find that such clouds may explain the observed EWDF if the halo velocity distribution function is as steep as that advanced by Klypin et al. (1999). Observations are best explained when individual halos have sub-halos that occupy the flanks of the “parent”. A picture emerges in which growth by accretion of sub-halos is possible. Further analysis suggests that the mass distribution about a cloud may extend significantly farther than the virial radius. Accounting for the total void mass density remains an outstanding problem.

Subject headings: intergalactic medium — quasars:absorption lines – dark matter – galaxies:halos

1. INTRODUCTION

Among the illuminati of cosmology, a paper that proposes to study Ly α clouds in voids, and further seeks to model them as remnants of sub-galactic perturbations, is likely to be viewed as an anomaly; N-body/hydro simulations have had such success in reproducing the detailed nature of the Ly α forest (*e.g.*, Miralda-Escude et al., 1996; Hernquist et al., 1996; Riediger et al., 1998; Cen & Ostriker, 1999; Davé et al., 1999; Davé & Tripp, 2001), that seriously considering a different picture is nearly unthinkable.

In these simulations, Ly α absorbers are *not* physically associated with discrete small halos; rather, they arise in large diffuse sheets or filaments (*e.g.*, Bi, 1993; Weinberg et al., 1997; Miralda-Escude et al., 1996; Davé et al., 1999). This view is supported by the conclusions of Dinshaw et al. (1997, 1998) regarding the hit/miss statistics of moderate redshift Ly α absorbers in double or group quasars. The possibility that these hit/miss statistics could instead be the signature of the clustering of small clouds was considered, and rejected without a thorough analysis (Weinberg et al., 1997)¹. Nor are Ly α clouds expected to be found in voids at $z \approx 0$ in any significant numbers, for in voids, the diffuse filaments expand with the Hubble flow and disperse to below the current limits of detectability at redshifts $z \lesssim 1$ (Riediger et al., 1998; Davé et al., 1999). Nevertheless, there exists now some considerable history of detections of low-redshift Ly α

clouds in voids (Morris et al., 1993; Stocke et al., 1995; Shull et al., 1996; Tripp et al., 1998; Penton et al., 2000a; McLin et al., 2002), suggesting that perhaps void clouds are not as rare as the simulations would imply. Likewise, the discovery of compact high velocity clouds (CHVCs) in the galactic neighborhood (Braun & Burton, 1999), which are successfully modeled as partially held by dark matter (Blitz et al., 1999; Sternberg et al., 2002), suggests that sub-galactic halos with associated H I gas may not be as unlikely as previously thought.

At issue is not just the specific disposition of dark matter and baryons in vast, dark, under-dense regions. The observations of Ly α clouds at low-redshift, where complete galaxy catalogs can be used to calculate their relative isolation, may provide a crucial test of the N-body simulations that play such a central role in informing our picture of process on the cosmic scale.

Simulations have effectively been calibrated by the use of the high-redshift Ly α forest. Under the assumption that dark matter (DM) can be characterized by a 3-dimensional power spectrum $P(k)$ (Bi, 1993; Croft et al., 1998), and that gas traces DM except at the smallest scales, where pressure forces are thought to be important (Bi, 1993), $P(k)$ is derived from high-redshift Ly α forest spectra, and used to model the initial conditions of simulations. The Ly α forest thus became a testing ground for simulations, enabling researchers to gradually refine their code to a point that there is now excellent agreement with observations of a wide range of Ly α forest properties (Miralda-Escude et al., 1996; Hernquist et al., 1996; Riediger et al., 1998; Cen & Ostriker, 1999; Davé et al.,

¹However, in unpublished work, Manning (2000) produced a good fit to the hit/miss statistics over a range of 10 kpc to 1 Mpc using discrete Ly α clouds clustered around small galaxy groups of physical extent ~ 750 kpc (*e.g.*, “Local Groups”).

1999; Davé & Tripp, 2001). These simulations show structure formation and movement of matter from low, to high density regions in response to peculiar gravitational fields. For instance, Cen & Ostriker (1999) use an open CDM model to follow the transferral of matter from underdense, to overdense regions, showing that over 90% of the mass in overdense (which we will later refer to as “shocked”) regions at $z = 0$ arrived after $z = 3$.

The challenging task of following the movement of gas in a simulated cosmological context is handled by concentrating baryonic and dark mass into baryon and dark matter “particles”, typically of mass $\sim 10^8$, and $\sim 10^9 M_\odot$, respectively (Katz et al., 1996; Hernquist et al., 1996; Davé et al., 1999). Due to this coarseness, small galactic and sub-galactic halos cannot be represented. Thus, the baryons that could have been associated with smaller halos are distributed in a smooth manner through the large diffuse structures. However, the response of the particles to gravity produces convergent motions which are interpreted as absorption lines – an effect known as the “fluctuating Gunn-Peterson effect” (Croft et al., 1998). Artificial spectra are typically extracted by smoothing groups of particles with a spline kernel with a radial scale that is dependent on the density (Katz et al., 1996) so that gas resolution varies from ~ 5 to $\gtrsim 200$ kpc for high, and low density regions, respectively (Hernquist et al., 1996). Thus, even if sub-galactic halos could be resolved, the dynamics of the behavior of baryons in the halo could not be realistically represented since the distribution of gas is determined completely by the spline function, which has no physical foundation.

In attempting to characterize the nature of the evolution of structure seen in simulations, two broad types of environments are detected. In Riediger et al. (1998) these environments are characterized as “shocked” and “unshocked”, while in Cen & Ostriker (1999), they are “warm/hot”, and “warm”. In either case, the filling factors, and the physics contributing to the physical state of the gas are approximately the same. The clouds in warm/hot, or shocked regions are collapsing structures, and are shock heated, while the warm, unshocked clouds characterize underdense regions in which gas is expanding with the Hubble flow, and is hence adiabatically cooled. In Cen & Ostriker (1999), the collapsing regions are thought to comprise about 10% of the volume of the universe at the present time. In the simulations of Davé et al. (1999) and Davé & Tripp (2001), clouds at high redshift populate both overdense and underdense regions, but for $z < 1$, absorbers are thought to arise in regions that are overdense by factors of 12 to 100; stronger lines originating close to galaxies, and weaker lines distributed in the diffuse filamentary structure.

At $z \sim 3$, the situation is different; the apparent lack of a modulation in the incidence of Ly α absorbers on velocity scales appropriate to galaxy superclusters or voids in high-redshift spectra prompted Carswell & Rees (1987) to conclude that voids in the Ly α cloud distribution can fill no more than 5% of the universe at $\langle z \rangle \simeq 3.2$, a result corroborated by others. However, the area is murky (see the review by Rauch (1998) for a discussion) since how one defines a Ly α cloud void depends on an arbitrary detection threshold.

However, the movement of this proto-void material toward mass concentrations will tend to evacuate them. Simulations of voids by Mathis & White (2002) suggest that no galaxy of any size is expected to currently populate voids of size $\sim 10 h^{-1}$ Mpc. However, studies show that there are much larger voids, with an average diameter greater than twice as large (*e.g.*, Hoyle & Vogeley, 2002; El-Ad & Piran, 2000). But void simulations of Arbabi-Bidgoli & Müller (2002) appear to imply that larger voids have generally lower densities. However, the relatively large galaxy density within the huge Boötes void (Dey et al., 1995), and the subsequent detection of other galaxies in 21 cm emission (Szomoru et al., 1996a,b), suggests that larger voids may retain halos when smaller voids may not.

The assumption that baryons trace a diffuse DM distribution, and not smaller, sub-galactic potentials, can, in principle be tested by the search for Ly α absorbers in local voids. For, if absorbers are diffuse, they will have expanded with the Hubble flow and now be so diffuse that they are unobservable (*e.g.* ?), while if they are held by sub-galactic halos, the gravitational potentials may be sufficient to restrain the evaporation of baryons and produce absorbers.

Observations of low-redshift Ly α clouds, aided by galaxy catalogs, can be used to determine the relative isolation of clouds, and may thus help to resolve these issues. For instance, Hubble Space Telescope (HST) spectra have detected numerous H I clouds for which no nearby galaxy was found (Morris et al., 1991, 1993; Stocke et al., 1995; Shull et al., 1996; Tripp et al., 1998; McLin et al., 2002). However, the methodology used by these investigators, though useful for gaining insight into the low redshift universe, does not facilitate the study of void clouds in any systematic way. For, “nearest neighbor” measures of a cloud’s isolation weights galaxies equally, whether dwarf or giant, and so lacks the sensitivity to mass that is intuitively attached to the concept of isolation.

A new method for resolving the environments of Ly α clouds is presented in Manning (2002) (hereafter Paper 1). It uses ambient tidal fields, calculated from galaxy catalogs, as a relative measure of a cloud’s isolation, and thus weights the effects of galaxies by their mass, and by the inverse cube of the distance. Clouds can then be sorted by their degrees of isolation. A catalog of clouds can, for instance, be divided into two; one sub-catalog with clouds abiding in ambient tidal fields less than some arbitrary tide \mathcal{T}_{lim} , and one with tide greater. The analysis of sub-catalogs into distribution functions can then be undertaken. It was found that clouds in low tidal field environments display significantly different characteristics than those in high tidal field environments.

When represented in a log-log plot, the equivalent width distribution function (EWDF) is accurately fit by a power-law. The left-hand illustration of Fig. 1 shows the EWDF of Ly α clouds, using all data irrespective of tidal field (heavy solid line). The break in the distribution, seen at $\log(\mathcal{W}) \simeq 1.5$ ($\mathcal{W} \simeq 32$ mÅ, where \mathcal{W} is the rest equivalent width of the Ly α absorber in mÅ) is suggestive of two distinct populations of clouds represented in the data. The thin solid and dashed lines represent number weighted fits to the data at $\mathcal{W} \leq 32$ mÅ, and $\mathcal{W} \geq 32$ mÅ, respec-

tively. The values of the slopes are shown. These results strongly suggest that isolated clouds exist in a different kind of environment than un-isolated clouds.

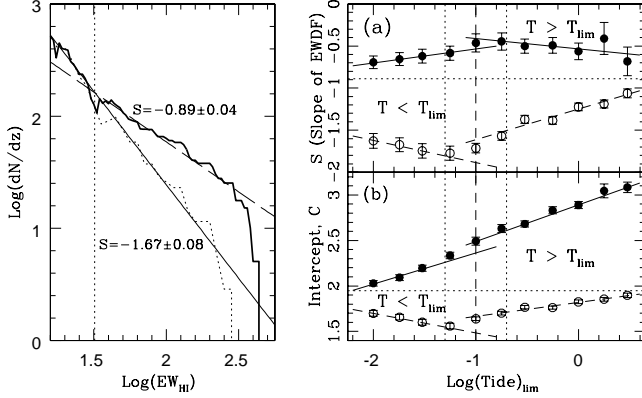


FIG. 1.— The left-hand figure shows the log of the mean cumulative line density (solid jagged line) as a function of the log of the EW for low- z Ly α clouds. It is evident that there is a broken power law, suggesting the existence of two populations of clouds. The spectral slopes, S , are shown for weighted linear fits to the mean EWDF for $W \geq 32$ mÅ (dashed line), and ≤ 32 mÅ (thin solid line). The latter fit matches the void EWDF slope well (dotted line). The vertical dotted line is at 32 mÅ. The right-hand figure shows the trends of fitting parameters, based on the model, $\log(dN/dz) = C + S \log(W/63\text{mÅ})$, with tidal field T_{lim} for void, and non-void catalogs. The upper panel of this figure shows the slopes, and the lower, the intercepts (log of line density at 63 mÅ). The horizontal dotted lines show the slope and intercept of the mean EWDF. Upper and lower sub-panels show non-void (tide as lower limit) and void (upper limit) EWDFs, respectively. The three vertical lines show the apparent range and center of the “transition zone” (see text). Note that characteristic slopes of void EWDFs (right-hand plot) are in agreement with the low EW slope of the mean EWDF (left-hand plot).

Note that the EWDF of *isolated* clouds (Fig. 1, left-hand plot, dotted line) closely matches the fit to the low EW part of the mean EWDF. This convincingly shows that isolated clouds constitute the “second” population (the low-EW side) seen in the mean EWDF. As it happens, there are virtually no low EW clouds in the un-isolated space (see *e.g.*, Fig. 13 in Paper 1). I parenthetically note that the line density of void clouds at $N_{HI} \simeq 10^{14}$ cm $^{-2}$ (*i.e.*, about 225 mÅ) is on order 7 per unit redshift. This is about 1/5 of the mean value; certainly not orders of magnitude less, as implied by simulations of Riediger et al. (1998).

Henceforth, I shall identify voids as regions that are isolated, where isolation is determined by the smallness of the scalar value of the summed tidal field (see §3 of Paper 1).

The line density of *void* clouds at $W \geq 15.8$ mÅ is $dN/dz \simeq 500$, and the spectral slope is steep $S \equiv d \log(d^2N/dz dW)/d \log W \lesssim -1.5 \pm 0.06$ (Paper 1, Table 2). In contrast, the slope of the volume-weighted (*i.e.*, mean) EWDF for $W \geq 32$ mÅ is $S \simeq -0.9 \pm 0.1$, while non-void clouds have quite flat EWDFs; $S \simeq -0.49 \pm 0.12$. Void clouds appear to actually dominate the mean EWDF at low EW.

The right-hand plot of Fig. 1 shows the trends of fitting parameters with changes in limiting values of tide T_{lim} , for both void (lower sub-panels) and non-void catalogs (upper

sub-panels). The tide is given in units of inverse Hubble time squared (see Paper 1) so that values are of order unity. There is a relatively narrow transition zone separating clearly distinct (linearly varying) trends in fitting parameters for void (low T), and non-void (high T) environments (note the vertical dotted lines). The transition zone provides a *phenomenological* basis for establishing the tidal field which separates void from non-void clouds. In this way, it is shown that the space containing void-type clouds fills $\sim 86^{+5}_{-11}\%$ of the universe (see Manning (2003) for more details). This is in good agreement with the 90% filling factor implied by Cen & Ostriker (1999).

I summarize these introductory comments by noting that (1) N-body/hydro simulations appear to predict that the great majority of low- z Ly α clouds are in the diffuse filamentary structure around galaxies, and not in voids. (2) The environmentally-resolved observations of Ly α clouds in Paper 1 show that most observed clouds lie in the unshocked void region, even without corrections for the much smaller redshift coverage of spectra at high sensitivity². (3) The lack of the ability to resolve cloud halos in N-body/hydro simulations may be the principal cause for the inability to predict the existence of this population of void clouds.

The foregoing tentative conclusions already throw suspicion on some of the results of the simulations. Is it that simulations fail to predict void clouds entirely? Two questions need to be answered; first, can diffuse clouds, expanding with the Hubble flow, explain the observed void clouds? Secondly, if not, can sub-galactic halos provide the gravitational potential needed to retain enough gas to produce detectable absorption systems? This is, in short, the purpose of this paper.

The paper is organized as follows: In §2 I investigate whether diffuse sheets of gas are capable of explaining the observed void EWDF, as envisioned in simulations. I find that diffuse sheets expanding with the Hubble flow are not consistent with observations. The remainder of the paper assumes the clouds are associated with sub-galactic halos, and that baryons are subject to pressure gradients after the reionization of the universe, and tend to expand away from their halos. In §3 I present a general analytical treatment of spherical clouds to show the relationship between the baryon density profile and the slope of the column density spectrum. In §4 I introduce the hydro/gravity simulation that will chart the evaporation of baryons from dark matter halos, in response to the re-ionization of the universe. These halos are initially viewed as fully formed and not accreting. In §5 I present the results of these simulations, based on a range of halo circular velocities and two halo types. Section 6 presents a series of strategies for fitting model column density spectra to the observations of Paper 1. In §7 I allow that clouds may accrete sub-halos, and so grow continuously from $z = 6.5$ to the present; the products at $z = 0$ are presented, and the results are compared to those with fixed halos. In §8 I reconcile Doppler parameters of model absorbers with those of the observed void clouds. In §9 I summarize my findings.

2. CAN DIFFUSE VOID CLOUDS EXPLAIN OBSERVATIONS?

² “High sensitivity” means sensitivity to very low EWs.

To determine the nature of void clouds under the current paradigm, one needs to know the fraction of neutral hydrogen atoms. Assume that clouds are optically thin, and immersed in a radiation field with an average flux $J_\nu = J_0(\nu/\nu_0)^{-\alpha_s}$, where $\alpha_s \sim 1.8$ (Zheng et al., 1997; Shull et al., 1999) is the spectral index shortward of the Lyman limit ν_0 . For the local universe, I assume,

$$J_0 = 1.3 \times 10^{-23} \text{ erg cm}^{-2} \text{ s}^{-1} \text{ Hz}^{-1} \text{ sr}^{-1}, \quad (1)$$

(Shull et al., 1999). For ionization equilibrium,

$$n_{HI} = n_H n_e \frac{\alpha_H^{(A)}}{\Gamma_{HI}} \quad (2)$$

(Osterbrock, 1989), where $\alpha_H^{(A)}$ is the case-A recombination rate coefficient appropriate for diffuse clouds. The photoionization rate is given by,

$$\Gamma_{HI} = 4\pi \int_{\nu_0}^{\infty} \left(\frac{J_\nu}{h\nu} \right) \sigma_\nu d\nu \approx 3.24 \times 10^{-14} \left(\frac{J_{23}}{1.3} \right) \text{ s}^{-1}, \quad (3)$$

where $J_{23} = J_0/10^{-23}$, and $\sigma_\nu \simeq \sigma_0(\nu_0/\nu)^3$ represents the hydrogen cross-section for absorption of a photon of frequency $\nu \leq \nu_0$, where $\sigma_0 = 6.4 \times 10^{-18} \text{ cm}^2$.

The expected neutral fraction is, from Eq. 2,

$$f_{HI} \equiv \frac{n_{HI}}{n_H} = 8.97 \left(\frac{1.3}{J_{23}} \right) \left(\frac{\alpha_H(T)^{(A)}}{2.51 \times 10^{-13}} \right) n_H. \quad (4)$$

Note that in a highly ionized plasma, $n_e \simeq n_H(1 + 2\chi)$, where $\chi = n_{He}/n_H \simeq 0.079$. Given that $\Omega_m = 0.3$, $\Omega_b/\Omega_m = 0.1$, and $Y_p = 0.24$, the hydrogen density is $n_H = 5.745 \times 10^{-7} h_{75}^2 \Omega_{cl} \text{ cm}^{-2}$, where Ω_{cl} is the total mass density of a cloud in units of the critical. Given $\Omega_m = 0.3$, the mean hydrogen density is

$$\bar{n}_H = 1.725 \times 10^{-7} h_{75}^2 \text{ cm}^{-2}, \quad (5)$$

For $T = 20,000 \text{ K}$, $f_{HI} = 1.55 \times 10^{-6} h_{75}^2 \Omega_{cl}$.

I note that the time-scale for ionization equilibrium is small;

$$\tau_{eq}^{ion} = \frac{1}{\Gamma_{HI}} \simeq \frac{1 \times 10^6 \text{ yr}}{J_{23}}. \quad (6)$$

Thus, ionization equilibrium is a safe assumption.

Now assume that large relatively homogeneous clouds exist in voids, as generically predicted by simulations, and that they are producing the isolated absorbers discovered in Paper 1. Assume that $\Omega_V/\Omega_m = 0.3$ (where Ω_V is the total mass density in voids). From Eq. 4, the neutral fraction is,

$$f_{HI} = 9.38 \times 10^3 n_H T^{-0.702} h_{75}^2, \quad (7)$$

where the index of T is the slope of the recombination coefficient (Osterbrock, 1989).

Davé & Tripp (2001) derive a relation between the temperature and the density from simulated data,

$$T = 5000(\delta\rho/\bar{\rho})^{0.6} \text{ K} \quad (8)$$

The exponent, 0.6, is actually an increasing function of decreasing redshift and increases with reionization redshift,

but 0.6 appears consistent with $z = 0$ values (Hui & Gnedin, 1997). According to Eq. 4 of Davé & Tripp (2001), $\delta\rho/\bar{\rho} \approx 12(N_{HI}/10^{14})^{0.7}$ at $z = 0$. The over-density required to produce a column density $N_{HI} = 10^{12.5} \text{ cm}^{-2}$ is $0.379 \bar{\rho}_H$, or $6.54 \times 10^{-8} h_{75}^2 \text{ cm}^{-3}$. With Eq. 8 I derive a temperature $T = 2794 \text{ K}$. Substituting this into Eq. 7, the neutral fraction of hydrogen is found to be $f_{HI} = 8.50 \times 10^{-6}$. Thus the length of the column needed to produce the absorber is,

$$l = \frac{N_{HI}}{n_{HI}} = \frac{N_{HI}}{f_{HI} n_H} \simeq 1.85 \text{ Mpc}. \quad (9)$$

If the filament is expanding with the Hubble flow, then the velocity width, ignoring thermal broadening, would be $\sim 140 \text{ km s}^{-1}$. Because the background mass density in voids is expected to be about an order of magnitude less than in the filamentary medium surrounding galaxies, the frequency of fluctuations of amplitude $\delta\rho/\bar{\rho} = 0.379$ will be very much smaller in voids than in non-void regions.

For $N_{HI} = 10^{13} \text{ cm}^{-2}$, $\delta\rho/\bar{\rho} \simeq 1.07$, $f_{HI} \simeq 8.23 \times 10^{-6} \text{ cm}^{-2}$, $T = 5207 \text{ K}$ and $l \simeq 2.14 \text{ Mpc}$. The implication is clear; absorbers formed in this fashion would be seen only as very broad troughs. The Hubble flow across l would then be well beyond the values found in the Space Telescope Infrared Spectrograph Echelle spectra (Davé & Tripp, 2001). In GHRS spectra with resolution is $\sim 19 \text{ km s}^{-1}$ (Penton et al., 2000a), void clouds have Ly α Doppler parameters, $b \sim 30 \text{ km s}^{-1}$ (Paper 1), probably large by a factor of ~ 2 due to resolution problems, and the presence of components (Shull et al., 2000). Thus void clouds have Doppler parameters only 1/5 to 1/10 as large as that which diffuse sheets would produce in voids.

In conclusion, it appears clear that the detected void absorbers must be either significantly denser than the mean density (*i.e.*, $\rho/\bar{\rho} \approx 10$), or the velocity field of the baryons must be strongly convergent with respect to the Hubble flow, or both. Neither of these conditions is consistent with the model of void clouds as diffuse baryonic slabs expanding with the Hubble flow. Thus, observations appear to be in conflict with the paradigm promoted by the N-body simulations as applied to Ly α clouds.

In the following section we begin our analysis of sub-galactic perturbations as a parent population for void clouds.

3. AN ANALYTIC TREATMENT OF SPHERICAL CLOUDS

If homogeneous slabs of gas expanding with the universe cannot explain these clouds, then what might? I hypothesize that absorbers stem from sub-galactic perturbations that were massive enough to restrain the outflow of gas from the dispersive tendencies of the Hubble flow and the pressure gradients that result from the ionizing background. I start with an analytic treatment of clouds taken as baryons held within a “mini-halo” Rees (1986).

Clouds whose evaporation is restrained by a centrally condensed halo of dark matter will have a radial density gradient. If such clouds can be roughly approximated by power law density profiles, their ionization structure, and column density spectra can be calculated.

3.1. The H I column density of spherical clouds

I initially assume that the baryons of a cloud have a spherically symmetric power-law distribution with index ϑ ;

$$\rho(r) \propto r^{-\vartheta}. \quad (10)$$

Eq. 4 shows that $n_{HI} \propto n_H^2$. The H I column density produced at projected radius r_p from the cloud center is,

$$N_{HI} = \int_{-\infty}^{\infty} n_{HI}(r) dl, \quad (11)$$

where l is constrained by the equation $r^2 = l^2 + r_p^2$. From Eqs. 4 and 11 we find,

$$N_{HI} = \frac{2\alpha_H^{(A)}}{\Gamma_{HI}} (1 + 2\chi) \int_0^{\infty} (n_H(r))^2 dl. \quad (12)$$

3.2. The Column Density Spectrum of Spherical Clouds

What column density spectrum would a cosmological distribution of such clouds produce? The cumulative column density spectrum may be broken down by the chain rule,

$$f(N_{HI}) = \frac{\partial^2 \mathcal{N}(\geq N_{HI})}{\partial z \partial N_{HI}} = \frac{\partial^2 \mathcal{N}}{\partial z \partial r} \frac{\partial r}{\partial N_{HI}}, \quad (13)$$

where $\mathcal{N} \equiv n_{cl}(\geq N_{HI})$. The relative number \mathcal{N} of absorption systems produced by a spherically symmetric system with a column density $\geq N_{HI}$ at projected radius r_p has a derivative, $\partial \mathcal{N} / \partial r_p \propto 2\pi r_p$. By Eqs. 2 and 10, $n_{HI} \propto r^{-2\vartheta}$. Then by Eq. 11,

$$N_{HI} \propto r_p^{-(2\vartheta-1)}. \quad (14)$$

Carrying out the derivatives in Eq. 13 and simplifying,

$$f(N_{HI}) = \frac{\partial}{\partial N_{HI}} \left(\frac{\partial \mathcal{N}}{\partial z} \right) \propto N_{HI}^{-(2\vartheta+1)/(2\vartheta-1)}, \quad (15)$$

which is the differential distribution.

The cumulative column density distribution has a slope larger by 1;

$$\mathcal{S} = \frac{2}{1 - 2\vartheta}, \quad (16)$$

The inversion of this yields,

$$\vartheta = -\frac{1}{\mathcal{S}} + \frac{1}{2}. \quad (17)$$

These two equations provide an important diagnostic of the observed column density spectrum (CDS) if we are to interpret it as produced by discrete, spherically distributed clouds, because it determines the cloud density profile that is consistent with a given CDS slope. Note that the steeper the index of the density profile ϑ , the flatter the spectral slope \mathcal{S} . For instance, the observed slope of the void cloud EWDF, $\mathcal{S} \simeq -1.5$ can be explained if $\vartheta \simeq 7/6$; *i.e.*, $\rho \propto r^{-1.17}$, while the slope for non void clouds ($\mathcal{S} \simeq -0.5$) is explained if $\rho \propto r^{-2.5}$.

4. NUMERICAL SIMULATION OF CLOUDS

For baryons associated with dark halos, it is not expected that baryons would follow their halo mass distribution at late times (e.g., Barkana & Loeb, 1999) – one might expect a flatter distribution owing to the effects of evaporation. As noted above, the steep EWDF of void clouds (Fig. 1) imply a relatively flat density profile; this may be a measure of the effects of reionization on baryons held by small dark matter (DM) halos. These considerations suggest that the clouds producing the absorption in voids have evolved into a rather flat density profile. A more accurate view of the probable profiles of such clouds may be achieved by a cosmological simulation of the response of DM-held clouds to reionization.

I propose to follow in detail the likely evolution of baryons in clouds gravitationally held by dark halos before reionization ($z \simeq 6.5$, Djorgovski et al., 2001). As noted above and in Paper 1, 3-D simulations suffer from space- and mass-resolution problems when small-scale structures are of interest, making it difficult to separate actual physical results from numerical artifacts. When small-scale structure needs to be studied, a 1-D code may provide a solution to the problem. I acquired a copy of a 1-dimensional Lagrangian hydro/gravity code of Thoul & Weinberg (1995) courtesy of one of its authors, (A. T.), and adapted it to the needs presented by the problem posed above. Among the adaptations made was the transformation from Einstein-de Sitter universe to a flat FRW ($\Lambda = 0.7$) with $h = 0.75$, and the writing of initializing routines for various halo models. These are consistent with the parameters used in Paper 1. A cosmic baryon ratio $\Omega_b/\Omega_m = 0.1$ is assumed.

4.1. Nature of 1-D Code

The code sets the value of the gravitational constant G to unity. In addition, it sets a mass scale, $\widehat{M} = 1.0 \times 10^{11} M_\odot$, and a length scale $\widehat{L} = 1.0 \times 10^{12}$ AU, or 22.592 kpc, mandating a time scale $\widehat{t} = 5.042 \times 10^{15}$ s, or ~ 160 Myr.

4.1.1. Governing physics

The equations, and related details of the computational scheme that forms the basis for tracking the evolution of the clouds are detailed in Thoul & Weinberg (1995). The basic components are recapitulated as follows. Ionization equilibrium is assumed because its time-scale is smaller than the time-scales of interest. The energetic gain Γ from photoionization of H I, He I and He II by UV photons is calculated on the basis of self-consistent concentrations of these components. We assume that the spectral index above the Lyman limit follows the relation, $J_\nu = J_0(\nu/\nu_0)^{-\alpha}$, where $\alpha = 1.8$, (e.g., Zheng et al., 1997; Shull et al., 1999). The redshift variation of $J_0(z)$ is adapted from Thoul & Weinberg (1995), and is shown graphically in Fig. 2. The radiative losses, Λ , are found by summing the cooling rates from collisional excitation and ionization, recombination, and bremsstrahlung, given the ionic abundances and the density (Thoul & Weinberg, 1995). In the Lagrangian code, bin boundaries for baryons respond to the effects of pressure differentials and gravitational potential gradients. The change in the internal

energy per unit mass u with time is then,

$$\frac{du}{dt} = \frac{p}{\rho_g^2} \frac{d\rho_g}{dt} + \frac{1}{\rho_g} (\Gamma - \Lambda), \quad (18)$$

where the first term on the right hand side is the adiabatic loss; p is the pressure, and the g -subscript refers to corresponding values for gas-bins. Shocks occur when motions are convergent. The artificial viscosity technique of Richtmyer & Morton (1967) is used, adjusted to spread shocks over 4 or 5 shells, helping to ensure energy conservation (Thoul & Weinberg, 1995). The pressure is given by the equation of state,

$$p = \frac{2}{3} \rho_g u. \quad (19)$$

The baryonic component responds to forces as follows,

$$\frac{dv_g}{dt} = -4\pi r_g^2 \frac{dp}{dm_g} - \frac{M(r_g)}{r_g^2}, \quad (20)$$

where $M(r_g)$ includes dark and baryonic mass, dp is the pressure differential over a Lagrangian bin, and dm_g is the gas mass contained therein.

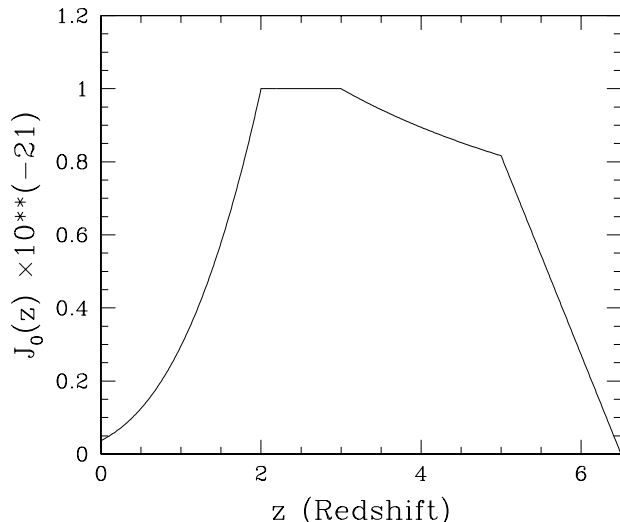


FIG. 2.— The prescribed average intensity at the Lyman limit, as adapted from Thoul & Weinberg (1995). In the interval $0 \leq z \leq 2.0$, $J_0(z) \propto J_0(1+z)^3$. The final results of simulations are fairly insensitive to the details of reionization.

The time-step for the simulation is determined by the smallest of a collection of time scales, including the dynamical timescale, the Courant, and the cooling time scales, and a time-scale to ensure that fluid shells do not cross. In addition there is a maximum length time-step of $10^{-3} \hat{t}$.

The minimum time-scale is frequently determined by the dynamical time-scale in the first few shells. When the timescale for cooling is much less than the dynamical time scale, shells are essentially in free-fall. This causes the central density to increase dramatically so that cooling time steps become extremely small. In response to this problem, when $\tau_{cool} \ll \tau_{dyn}$ the program “freezes” the shells in question, and refers the mass to a minimum radius, here, $r_{min} = r_c$ – essentially taking the mass in the shell out of gas form (we might speculatively suggest that gas

fragments and forms stars in the collapse zone). In practice, this does not occur for systems of circular velocity less than $v_c \lesssim 21$ or 24 km s^{-1} , for Navarro et al. (1996, 1997) (hereafter, NFW) and isothermal halos, respectively. Since this is an investigation of clouds and not galaxies, I ignore systems of larger circular velocity. I check that the point at which shells are frozen is physically realistic by monitoring the ratio of the diameter of the first Lagrangian bin to the Jeans length, given by

$$\lambda_J = \sqrt{\frac{\pi \gamma k_B T}{G \rho \mu m_H}}, \quad (21)$$

where γ is taken to be $5/3$, and μ is the mass per particle in units of the hydrogen atom, that approaches the value $\mu = 0.588$ at the low densities of model clouds at low to moderate redshifts. This indicator is found to approach unity shortly before the shells are frozen, indicating that the program is treating the problem correctly.

It is possible that starting with a less-relaxed halo, warmed by secondary infall at $z < 6.5$, halos of circular velocity high enough to collapse in this way under the current arrangement, would not collapse. This implies that clouds of somewhat larger circular velocity could exist without forming stars (see §7).

4.1.2. General Treatment of Dark Halos

Because the Thoul & Weinberg (1995) code was originally written for collapsing protogalactic clouds, the program’s treatment of DM is inappropriate for the present simulation. Instead, a dark halo overdensity is established and not allowed to change (these halos are to be specified below). It would be more proper to project a dark halo as it would be at a high redshift, growing somewhat by secondary infall, so that the end product is consistent with the specified circular velocity. However, of this there are two views; one states that the halo of a small cloud is in place by $z = 6.5$ (see Wechsler et al. 2002)³, so that most of the response to absorbed radiant energy is at redshifts in which the total cloud mass is fairly stable. In this scenario, therefore, assuming a fixed halo circular velocity can only modestly minimize the final extent of cloud expansion due to its greater average potential. However, the other view is based on observations suggesting the growth of halos, even at late times. Therefore, after applying the analyses to fixed halos, we then allow halos to grow steadily by accretion of sub-halos, leading to a growth of circular velocity with time. These “grown” halos are subjected to the same analysis as the fixed halos, providing a plausible maximal range for reasonable models of halo growth.

The spherically symmetric conditions of the simulation presume that the halos are isolated from the influences of others. This approximation should be accurate for void clouds since the environment around them is expanding with the Hubble flow, and evaporation ejecta are not likely to interact with that of other isolated systems. However, it would not likely apply to non-void space because in the convergent flows of over-dense regions, cloud outflows may collide causing shocks, that violate the isolation and spherical symmetry assumed in this simulation.

³The virialized mass will grow in time, but that is only apparent growth since it results from the decline in ρ_{crit} with time.

4.1.3. General Initial Conditions

The initial conditions of model clouds are designed to make them dynamically stable. Because the central densities of clouds are supposed to approximate the density of the universe at the redshift of their formation (the canonical explanation for the high concentration parameters of small systems in relation to those of large systems found in simulated halos), I assume that the halos I model are already in place at $z = 6.5$. There may be some confusion on this issue because it is seen that the virial mass of even small halos continues to grow down to $z = 0$ (e.g. Bullock et al., 2001). However, the virial radius is approximately equal to the radius within which the average density is $\sim 200 \rho_{crit}$. Therefore, the decline in the background density with the expansion of the universe causes an expansion of the virial radius, resulting in an increase in the virial mass with time. Comparisons with code kindly lent from J. Bullock (“cvir.f”) show that, for clouds with $v_c \leq 25 \text{ km s}^{-1}$, there is very little increase in mass, or decrease in the concentration parameter over and above that which naturally results from the expansion of the universe. Therefore, from the standpoint of current thinking, assuming that the halos were in place at $z = 6.5$ should be non-controversial. However, from the standpoint of the isothermal model, this may not be true. Accordingly, we do investigate halos which grow steadily in §7.

In deciding the initial conditions of the gas associated with a “fixed” dark halo (i.e., fixed circular velocity v_c and overdensity profile), it is important to note that at high redshift the baryonic cloud is immersed in a critical density background with density comparable to that of the cloud. For, at $z=4.84$ the background density is 200 times the current critical density, thereby making the virial radius significantly smaller than at the present. Because baryons are dissipational, there is no way to separate the baryons that are part of the overdensity from those that are part of the background. In fact, what allows for the existence of a prolonged and stable overdensity is a distortion in the Hubble flow that is concentric about a point we would call the center of the cloud. Since these halos are immersed in a high-redshift universe, their overdensity exists by virtue of this deviation from the Hubble flow.

At the initialization stage, an outward motion is given to the gas that is less than, but gradually approaches the Hubble flow velocity as one considers radii farther from the cloud center in a manner such that the overdensity is stable in time. This is actually easier than it sounds, for one need only give an outward velocity such that the radial flux of gas is what it would be if the universe were flat and of critical density. Thus, at a given redshift z , the outward motion of gaseous matter v_g needed to maintain a density $\rho_g(r)$ at a distance r , for instance, should equal,

$$v_g(i) = H r(i) \Omega_b \rho_{crit} / \rho_g(i), \quad (22)$$

where the variables, H , Ω_b , and ρ_{crit} are evaluated at the redshift in question. This creates an overdensity that is stable within the Hubble flow (the peculiar velocity supports the overdensity). The dark matter is given the same peculiar velocity field. The velocity field that results can be expressed as proper radial motion (including the Hubble flow) as well as peculiar velocity, with the Hubble flow subtracted.

Because of the exigencies of a Lagrangian code, and the apparent lack of evidence for a truncation of halos at the virial radius, it was decided not to impose a radial truncation of the overdensity of halo models. The halos were extended to a distance at which the average internal overdensity in units of the current critical density was $\bar{\rho} = 2 \rho_{crit}$, equivalent to a distance of $\sim 2 \text{ Mpc}$ from an \mathcal{L}^* galaxy with an isothermal (hereafter referred to as ISOT) model halo. Later, when estimates of the average density contributed by clouds are required, it will be possible to impose a truncation radius, such as that featured in Paper 1. It should be borne in mind, however, that there are no features in the simulation products that would imply that the mass is truncated at any characteristic radius, nor does the preponderance of observational evidence (see below) require it; only N-body simulations suggest something like that might be required. Since the extent of gravity is infinite, halos have the tendency to draw matter toward them incrementally at great distances.

Initially, baryons are taken to “follow” the DM, so there is an inward peculiar gravity acting on the baryons. To restrain baryon collapse, I initially constrain the cloud to have a temperature such that the pressure exactly balances the peculiar gravity in each bin. This will not guarantee that clouds are static because cooling rates vary within the cloud, however, it is dynamically stable. For instance, if the simulation is started at $z = 10$, instead of 6.5, the baryons will “slosh” about within their halo, but when ionization begins, the cloud expands, producing a result remarkably similar to those with simulations begun at $z = 6.5$.

It turns out that the details of the temperature structure is relatively unimportant because, for clouds with virial temperature $T_{vir} \leq \text{few} \times 10^4 \text{ K}$, the cooling time-scale is large, suggesting that clouds are fairly stable before reionization. Further, the energy deposited upon reionization dwarfs the initial energy content, so that the effect of the initial temperature on cloud dynamics is insignificant. Other tests showed that the final state of the cloud is also quite insensitive to variations in the specific prescription for the onset of the ionizing flux (see Fig. 2). Thus, final results are sensitive only to halo type and circular velocity.

4.1.4. Initializing routines

In the initialization stage of the program, the halo model and its DM circular velocity are specified, and the total mass of the cloud in DM and baryons derived therefrom are calculated according to the cloud halo model, extending to a radius at which the internal over-density is 2 times the critical. This ensures a large enough scale to capture the relevant dynamics of expansion, and guarantee that all observable column densities occur within the cloud end-products. The mass is then divided equally into the number of Lagrangian bins to be used (generally, the number of gas bins are set to $n_g = 200$, and the dark matter divided into $n_d = 500$ bins). Then the initial radius at which these masses are found is determined by straightforward application of model relations (see §5.1).

This study considers halos which are isothermal as well as NFW halos. I do not truncate these halos at the virial radius because what is of interest is the mass distribution of the halos, rather their kinetic properties. Numerous studies now support the claim that there is no

sign of a drop in the index of the density profile beyond the virial radius, or for that matter, the NFW radius of maximum circular velocity (*e.g.*, Zaritsky & White, 1994; Zaritsky et al., 1997; Zabludoff & Mulchaey, 2000; McKay et al., 2002). In their study of weak lensing, McKay et al. (2002) show that the line-of-sight (LOS) velocity dispersion σ_r of satellite galaxies around 618 isolated host galaxies from the Sloan Digital Sky Survey is consistent with σ_r being constant over a range $100 \lesssim r \lesssim 500 h^{-1} \text{ kpc}$, and that the number density of satellites $n \propto r^{-2.1}$ over this range. This is very suggestive of a mass distribution that is not truncated; one not inconsistent with an isothermal mass distribution. To make the distinction clear, when I refer to a halo, I am referring to the mass distribution, rather than the mass in the virialized portion thereof. It is expected that the mass of the early halo will generate peculiar velocities in the surrounding universe, contributing to an enhancement of the density outside the virialized region of the halo.

The NFW Halo: The NFW halo is treated in considerable detail in Paper 1. Equations 34 to 40 of Paper 1 describe the derivation of the scaling relations of the model, which are necessary for calculating halo parameters as a function of halo circular velocity. A formula for the mass as a function of distance is the basis for determining the bin distributions and calculating density within the bins,

$$M_{\text{NFW}}(r) = \frac{4\pi}{3} 200\rho_{\text{crit}} r_{200}^3 \left\{ \frac{\log_e(1 + r/r_s) - \frac{r/r_s}{1+r/r_s}}{(\log_e(1 + c) - c/(1 + c))} \right\}, \quad (23)$$

where r_s is the scale length, r_{200} is the assumed virial radius enclosing a density of $200\rho_{\text{crit}}$, and c is the concentration parameter defined by, $c \equiv r_{200}/r_s$, where r_s is the scaling radius, and r_{200} is the density at which the average internal density is 200 times the critical density, or, loosely, the virial radius. The concentration parameter is a function of the halo circular velocity, and was derived from relations taken from NFW (see §5.1.2 of Paper 1),

$$c \simeq 132.3 v_{\text{max}}^{-0.393}, \quad (24)$$

where v_{max} is the maximum halo velocity, which occurs at a distance, $r_{\text{max}} \simeq 2.16r_s$. Be aware that there is significant dispersion in these relations, as they are average values derived from the results of computer simulations. The NFW halo has a cuspy core, with density approaching $\rho \propto r^{-1}$ as r goes to zero.

The Isothermal Halo: In Paper 1, the isothermal halo (which I will henceforth abbreviate as ISOT) was used to model the total mass of galaxies, and so required no internal structure to be stated. This study, however, requires an explicit core. I assume that the central non-singular core of the ISOT model has a density equal to that found by Firmani et al. (2001) in their investigation of the central densities of dwarf galaxies. I apply an exponential term to the density law,

$$\rho(r) = \frac{GK}{4\pi r^2} \left(1 - e^{-(r/r_0)^2} \right), \quad (25)$$

so that that there is a flat core of density $\rho_c \simeq 0.02 \text{ M}_\odot \text{ pc}^{-3}$, that constrains the core size r_0 , and also allows the mass

to approach a value $M(r) = \mathcal{K}r$ for $r \gg r_0$. I find that

$$r_0 = 0.3035 \times \left(\frac{v_c}{10 \text{ km s}^{-1}} \right) \text{ kpc}. \quad (26)$$

The simulation begins with the baryons “following” the DM distribution, and shortly thereafter they are subjected to an isotropic metagalactic flux whose amplitude at the Lyman limit $J_0(z)$ is shown in Fig. 2.

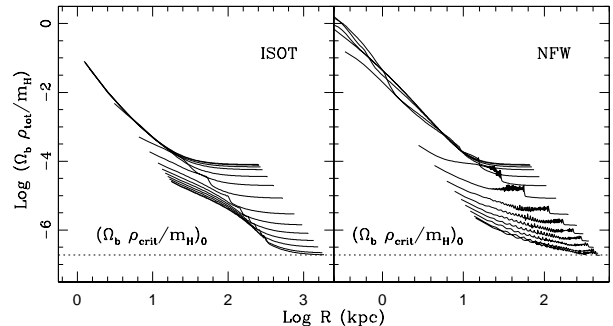


FIG. 3.— The evolution of an isothermal cloud (left panel), and an NFW cloud (right panel), both with $v_c = 21.1 \text{ km s}^{-1}$. The log of the baryon number density is shown as a function of the log of the cloud-centric radius at an arbitrary series of times (see text). The simulation starts at $z = 6.5$ (topmost lines) and proceeds to $z = 0$. The NFW halo (right-hand plot), being more strongly concentrated, has a smaller first gas bin, and higher density there, but a lower total mass. Note the outflowing wave that is stronger in the NFW halo than the ISOT.

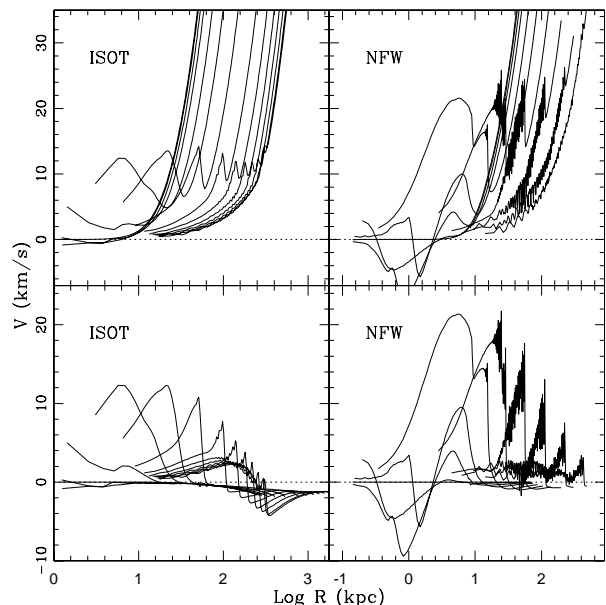


FIG. 4.— The proper velocity (upper panels) and the peculiar velocity (lower panels) for ISOT halos (left panels) and NFW halos (right panels) at arbitrary points from $z = 6.5$ (left-most line) to $z = 0$ (right). As in Fig. 3, velocities are shown as a function of the log of the system-centric radius. The cloud halo velocity shown in this experiment is $v_c = 21.1 \text{ km s}^{-1}$. This NFW halo has acoustic oscillations on time-scales of order 600 Myr. The ISOT model produces relatively minor shocks and oscillations.

4.2. Behavior of Baryon Clouds after Reionization

The program advances in steps and needs about 15,000 time steps to get to $z = 0$. The program prints out data every 20 steps, leaving about separate 750 files. Figures 3 and 4 show the reaction of a large cloud ($v_c \simeq 21.1 \text{ km s}^{-1}$) to reionization. The time steps at which the distributions were sampled are arbitrary; chosen to give a sense of the dynamics and to avoid confusion. The chosen files are roughly geometrically arranged (*e.g.*, using files #1, 2, 5, 10,...) until (for ISOT) reaching file number one hundred, then continued to sample at each 100 steps to the last step near 750. For NFW halos the doubling continues to $z = 0$ to avoid the confusion of overlapping plots. A sense of the redshift can be had by recognizing that the density at the extreme edge of the cloud is $\Omega_m \rho_{crit}/m_H \propto (1+z)^3$.

The principal distinction between the ISOT and NFW density profile evolution is that ISOT has a softer outflowing wave, and a significantly larger central density at the conclusion of the run. The NFW halo, which is very concentrated, sends out a strong wave of expansion that introduces a shock that reverberates back into the inner cloud. The lower final central baryon densities of the NFW clouds, roughly a tenth of the ISOT clouds when comparing clouds of equal circular velocity, reflects its lower mass. The evolution of velocity profiles for halo models with $v_c = 21 \text{ km s}^{-1}$ is shown in Fig. 4. It shows that the outflowing wave from the NFW halo has a significantly stronger amplitude – by almost a factor of two – accompanied by a strong oscillation of the inner cloud. The magnitude of the wave declines significantly in time for each model. The final peculiar velocities (lower panels) at large cloud-centric distances are only slightly negative for the NFW halo, while the more massive ISOT halo has produced a sizable negative peculiar velocity at late times just beyond the outflowing wave. Note, however, that the higher density gas internal to this still has a positive peculiar velocity. This discontinuity, here located at $r \simeq 260 \text{ kpc}$, is far beyond the canonical virial radius for this cloud ($r_{vir} \simeq 25 \text{ kpc}$).

4.3. Comparison of Program Output with Other Work

Data from simulations of clouds can be used to probe the trend of temperature with density as a function of redshift. In Fig. 5 is plotted the logarithm of the density (in units of $\Omega_b \rho_{crit}$) versus the log of the temperature at $z=0$ (skeletal), $z = 1$ (open circle), and 2 (open pentagon). The data at $z=0$ is taken from a maximal ISOT halo with $v_c = 23.7 \text{ km s}^{-1}$ (5-pointed stars) and with a smaller halo, $v_c = 13.3 \text{ km s}^{-1}$ (crosses). Note that the locus of points from the smaller cloud is marginally cooler than that from the larger cloud because the smaller cloud may expand more freely, increasing the adiabatic cooling. The heating produced by the outflowing shock (or cooling following its passage) can be readily seen in the $z = 1$ and 2 plots (note the discontinuity), though by $z = 0$ the wave has passed beyond the outermost point.

Also in Fig. 5, these program outputs are compared with a result from Fig. 3b of Hui & Gnedin (1997), based on the output of a 3-D hydro code (dashed line, label *HG*, $z = 2$), which utilizes rapid reionization at $z = 7$ and a flat Λ model. Also shown is the relation implied by Eq. 8, as found in Davé & Tripp (2001) (solid line,

labeled *DT*), which represents the trends in the filamentary structure surrounding galaxies (*i.e.*, non-void space) at $z \simeq 0$. Note that the Hui & Gnedin (1997) trends ($z = 2$) appear to approach the trend for the results from the 1-D simulation *inside* the outflowing wave. However, the Davé & Tripp (2001) model appears to predict significantly larger temperatures at densities of a few or more. This is attributed to shock heating and bulk motions in this denser environment, said to be more pronounced at low redshift Davé & Tripp (2001).

Given the differing physical conditions that are probed by the 3-D (non-void) and the 1-D (void) simulations, the differences in predicted temperatures are not surprising.

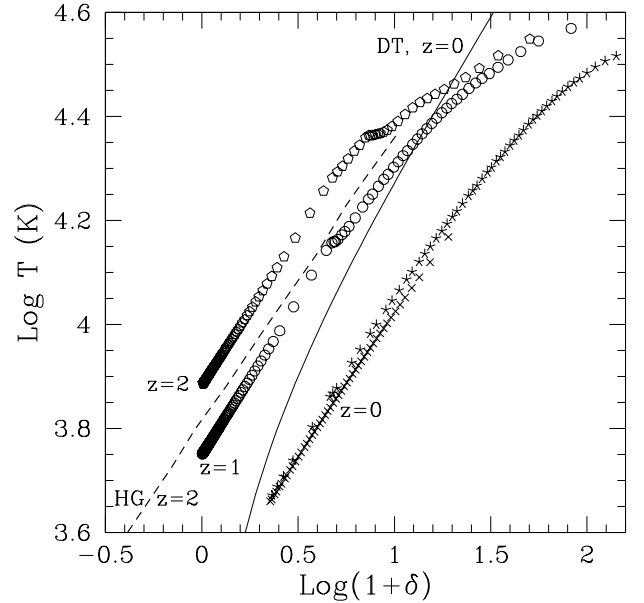


FIG. 5.— The logarithm of the temperature (in Kelvins) of cloud parcels as a function of the log of the over-density (in units of $\Omega_b \rho_{crit}$) for various redshifts. Symbols represent the present work, and labeled lines represent the work of Hui & Gnedin (1997), and Davé & Tripp (2001). The skeletal symbols show the variation of trends of temperature at $z = 0$ in large clouds (5-armed) vs. small clouds (4-armed), where smaller clouds are cooler as a result of the greater freedom a small cloud has to expand, and adiabatically cool. Open circles, and pentagons show trends for $z = 1$, and 2, respectively, for the large ($v_c = 23.7 \text{ km s}^{-1}$) cloud. See §4.3 for further discussion.

5. RESULTS AT REDSHIFT ZERO

The program is run for a range of cloud halo velocities v_c with bin-centers at,

$$v_c(n) = 5.31 \times 10^{0.05n} \text{ km s}^{-1}, \quad (27)$$

for $n=0$ to 13. These bins cover circular halo velocities of 5 to 25 km s^{-1} . Halos larger than this experience what appears to be the equivalent of star formation, *i.e.*, free-fall collapse in the central regions of the cloud. The cadence in Eq. 27 has 20 logarithmic steps in a decade of v_c .

Another form for designating the velocity bins is the following,

$$X_v(n) \equiv \frac{v_c(n)}{v_c^*} = \frac{v_c(n)}{144}. \quad (28)$$

One should notice that 144 km s^{-1} is the velocity of the dark halo of an \mathcal{L}^* galaxy that, when baryons are added to comprise 10% of the total, has a circular velocity of 161 km s^{-1} (see §5.1.1 of Paper 1).

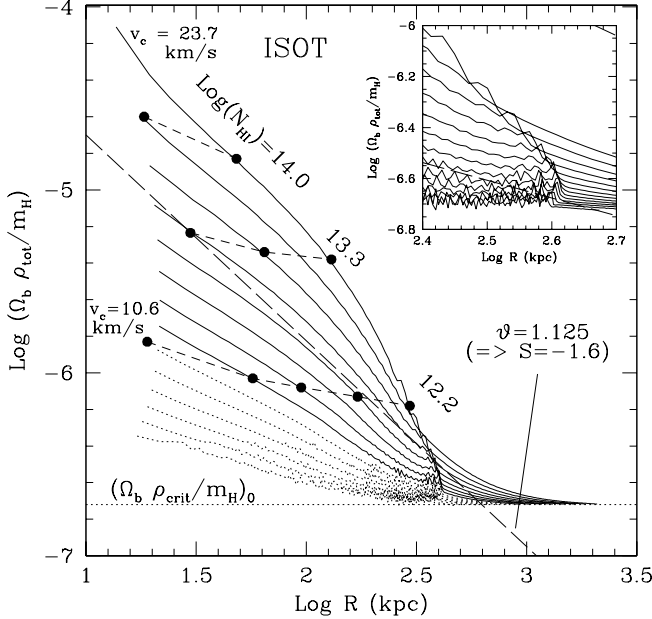


FIG. 6.— Final density profiles ($z = 0$) for the range of halo velocities for the ISOT model. The dashed line represents the slope of the density profile ($\vartheta = 1.125$) necessary to produce the observed slope $S \approx -1.6$ of the CDS for void clouds, (see §3.1). Clouds with circular velocity $v_c \gtrsim 10 \text{ km s}^{-1}$ have slopes that approximate this value inside $\sim 150 \text{ kpc}$. Profiles with dotted lines are undetectable in Penton et al. (2000a). The enlarged dots and short-dashed lines represent the radii where particular clouds give the stated column density (see log of column density labels). The inset shows the detail of the cloud outer edge showing that the self-gravity of the larger clouds has restrained the outflow wave for halos with velocity $v_c \gtrsim 10 \text{ km s}^{-1}$.

5.1. Model Halos at $z = 0$

The products of simulations for $z = 0$ are of special interest, for the density profiles, temperatures, and neutral fractions of hydrogen, will provide what we need to produce a model column density spectrum (CDS). The results strongly depend on the halo model.

5.1.1. ISOT density profiles

The $z = 0$ results of an ISOT simulation are seen in Fig. 6, where the smallest cloud $v_c = 5.31 \text{ km s}^{-1}$ is the bottom, dotted line. The smallest cloud to produce a detectable absorption line of $N_{\text{HI}} \geq 10^{12.4} \text{ cm}^{-2}$ is the bottom solid line, where $v_c = 10.6 \text{ km s}^{-1}$. The long-dashed line in the figure has a slope ϑ that is associated with a CDS slope $S = -1.6$ through Eq. 16, the observed slope of the void CDS. The labeled short-dashed lines show the radius at which selected column densities are detected, and the baryon density at the closest approach of the LOS. This will be discussed in detail in §5.3. Note that large clouds may produce low-column density absorbers at distances as large as 200 or 300 kpc, though the spectral slope they would produce would be significantly shallower than that observed in the void CDS of Fig. 1.

The inset of Fig. 6 shows an enlargement of the zone of the outflowing wave. For smaller halo velocities, the position of the wave at $z = 0$ scales directly with the core-radius, indicating the outflow is essentially unrestrained. However for $v_c \gtrsim 10.6 \text{ km s}^{-1}$ (8th from the top), the position of the wave is at progressively smaller radii, attributable to the cumulative effects of their massive halos. These effects are also seen in the peculiar velocity plot of the large ISOT halo in Fig. 4.

That neutral hydrogen mass of these halos can be straightforwardly calculated from the output of the code, and while not directly relevant to this study, it is relevant to 21 cm studies of high velocity clouds (HVCs), and is an opportunity to compare Ly α and HVCs. These data are presented in §7.

5.1.2. NFW density profiles

The NFW simulations to $z = 0$ are presented in Fig. 7. Gas density profiles are seen to be flatter than $\vartheta = 1.125$ outside $\sim 30 \text{ kpc}$. There is an apparent total blow-out phenomenon for clouds with $v_{\text{max}} \leq 10 \text{ km s}^{-1}$, and a blowout of the outer cloud for clouds smaller than $\sim 18 \text{ km s}^{-1}$. The smaller physical extent of the clouds has resulted in the expanding wave having traveled beyond the outermost Lagrangian bin except for the most massive cloud with $v_c = 21.1 \text{ km s}^{-1}$. The cloud with $v_c = 23.7 \text{ km s}^{-1}$, however, collapsed from the inside out, and would presumably form stars, and was therefore discarded as a model cloud. As we shall see, NFW halos do not produce observable H I columns in these simulations.

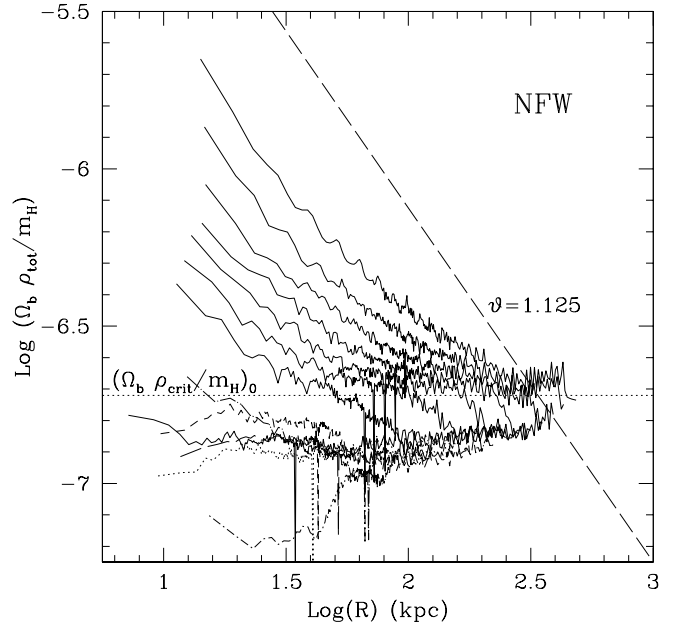


FIG. 7.— NFW density profiles evolved to $z = 0$ for $v_c = 5.3$ to 23.7 km s^{-1} . Note that low v_c clouds have expanded with such force that they are actually *underdensities* at $z = 0$. The dashed line has slope $\vartheta = 1.125$, that would produce a column density spectrum slope $S = -1.6$, approximately that of the void CDS.

5.2. The Nature of Model Absorbers

Here I discuss the method of extracting model absorption systems, and looking at the thermal and velocity structure of the absorbers.

5.2.1. Calculating cloud column density

Let us consider a line of sight through a particular ISOT cloud. Given an arbitrary targeted column density, we seek to find two consecutive bin radii that serve as impact parameters $r_p(i)$ and $r_p(i+1)$, at which column densities bracket the target column. One may then interpolate the solution. When the line of sight (LOS) velocity profiles of the model absorbers are analyzed, it is found that absorption systems typically have a strongly peaked central core, with broad wings that may add substantially to the calculated column density. This “background” is attributable to a Gunn-Peterson effect (Gunn & Peterson, 1965). Simulated clouds are hypothesized to be immersed in a gas of density $\Omega_b \rho_{crit}$, and under the UV flux utilized in these simulations (see Fig. 2 and Eq. 1), the neutral fraction of hydrogen gas of this density at $z = 0$ is found to be $f_{HI} \simeq 1.5 \times 10^{-6} \text{ cm}^{-3}$.

The simulated data is subjected to the same treatment as the observations. In the reduction of the observational data, a continuum is placed with respect to which the fluctuations of the spectrum, in zones not influenced by absorption or emission lines, are evenly balanced, above and below the continuum. Therefore, this background Gunn-Peterson effect is subtracted from the model absorber. Using the neutral fraction of this background gas, and the $z = 0$ background hydrogen density ($1.745 \times 10^{-7} \text{ cm}^{-3}$), yields a neutral hydrogen density in a cloud of total density $\Omega_m \rho_{crit}$ of $n_{HI} = 2.61 \times 10^{-13} \text{ cm}^{-3}$. The neutral column in a megaparsec is thus $N_{HI} = 8.04 \times 10^{11} \text{ cm}^{-2}$. In the Hubble flow, if we take 1 Mpc to be 75 km s^{-1} , there is a column “dispersion” of $dN_{HI}/dv = 1.07 \times 10^{10} \text{ cm}^{-2} \text{ per km s}^{-1}$, or $10^{12} \text{ cm}^{-2} \text{ per } 93.3 \text{ km s}^{-1}$. This provides a minimal approximation to the displacement of the continuum due to background neutral hydrogen. This background column density dispersion is scaled to the velocity of the extracted profile, and subtracted from the total column density to get an “observed” value.

The program finds the projected radius r_p at which a target column density occurs, and uses that to calculate the surface area of the cloud that will produce a column greater or equal to the target column. The utility of this parameter for deriving the column density spectrum will be demonstrated in §6.3.

5.2.2. Cloud temperature versus b -value

The temperature of a cloud is an important factor in predicting the Doppler parameters of model clouds. As shown in Fig. 5, the temperature of clouds vary systematically with density. I define the temperature of an absorption line as the temperature of its core. To do this I calculate the column density-weighted temperature within the range at which the differential column in the successive bins drops to half the maximum value.

Cloud outflows at $z = 0$ are generally quite small (of order ~ 2 to 7 km s^{-1}) compared to the observed b -values of clouds. Recall that the most likely Doppler parameter for void clouds with the GHRs data of Penton et al. (2000a) (see Paper 1, Fig. 6) is $b_{Ly\alpha} \simeq 30 - 35 \text{ km s}^{-1}$. If purely thermal, this would correspond to a temperature

of $T \simeq 70,000 \text{ K}$. I retrieve from the model lines a column density-weighted temperature for a range of columns N_{HI} , and a range of cloud velocities, all summed within the line FWHM. This will provide a theoretical lower limit to observed cloud b -values as a function of EW or column density. In fact, a fairly tight relationship between column density and temperature results from model clouds. These temperatures, for log-column densities of 12.5, 13.0, 13.5, and 14.0 are, 7800 K, 11600 K, 16900 K, and 27000 K, respectively. The range of temperatures at log-column 12.5 is fairly large ($\sim 300 \text{ K}$) because of a wide range of halo velocities that may produce the line, but it is smaller for large column densities since only a small range in cloud v_c may produce them. These data, transformed into a thermal b -value⁴, are plotted in Fig. 8 as open pentagons, and provide a theoretical lower limit to cloud b -values.

5.3. Transforming EW into Column Density

In order for observed absorption systems (EW in units of mÅ) to be compared with model results (column density in units of cm^{-2}), one needs to account for the self-blanketing effects of H I clouds. In this section I discuss transformations of the EWDF to a CDS, for this is required before model clouds may be compared to the observed EWDF.

If the cloud is quiescent and of uniform temperature, then the thermal broadening of the line will characterize the Doppler parameter b . A low-temperature cloud will deplete the continuum photons with wavelengths $\lambda = 1215.67 \text{ Å}$ in the cloud rest frame because of the large fraction of neutral atoms that can efficiently absorb at the Ly α resonance, and so produce an absorption system with lower EW than a hotter cloud of the same column density, which would not produce this “blanketing”. If there is well-developed turbulence such that at physical scales of the overturning regions, the column density is small in relation to the total column through the cloud, then this must be added in quadrature to the thermal b -value in order to arrive at the total b -value; $b = \sqrt{b_{therm}^2 + b_{turb}^2}$. If turbulence or virial motions exist on large scales, then the cloud should ideally be characterized by a superposition of independent Doppler parameters, rather than a single one.

The measurement of b from the Ly α line of an H I absorber (hereafter $b_{Ly\alpha}$) may reflect not only the line broadening effects of temperature and small-scale turbulence, but large-scale cloud motions, or physically associated sub-condensations; thus it is also a function of the resolution of the spectra.

For clouds with no large-scale motions, the line-blanketing effects in clouds can be characterized by the use of the relation of Chernomordik & Ozernoy (1993) that approximates the equivalent width of an absorber as a function of optical depth τ and the Doppler parameter b ;

$$\mathcal{W} = \frac{\sqrt{2}b\lambda}{c} \left\{ \log_e \left(1 + \frac{\pi}{2} \tau^2 \right) \right\}^{1/2}.$$

The optical depth $\tau = 1.497 \times 10^{-2} \lambda f_{12} N/b$, where the oscillator strength for Ly α is $f_{12} = 0.416$, and $\lambda = 1215.67$

⁴for hydrogen, $b_{therm} \simeq 0.128 T^{1/2} \text{ km s}^{-1}$

Å. Substituting, and solving for column density,

$$N_{HI} = 1.05 \times 10^{12} b \sqrt{\left\{ \exp \left[\frac{1}{2} \left(\frac{0.247 W}{b} \right)^2 \right] - 1 \right\}} \text{ cm}^{-2}. \quad (29)$$

This relation is claimed to be accurate within 10% for all optical depths $\tau < 40$. For small W ($W \lesssim 150$ mÅ), it reduces to the standard linear relation,

$$N_{HI} = \left(\frac{W}{54.43} \right) \times 10^{13} \text{ cm}^{-2}, \quad (30)$$

as noted in Penton et al. (2000b).

It is possible to separate the effects of the large scale motions influencing the $\text{Ly}\alpha$ line-width from the effects properly incorporated within the Doppler parameter by using observations of higher-order Lyman series absorbers and curve-of-growth analysis to arrive at the true b -value. Using the Far Ultraviolet Spectroscopic Explorer (FUSE), Shull et al. (2000) observed 12 clouds with $W \gtrsim 200$ mÅ. Results suggested that the intrinsic (thermal) line widths of the clouds were generally much smaller than that measured from the $\text{Ly}\alpha$ line. For the clouds with modest to small uncertainties in b -value, the average reduction from $b_{Ly\alpha}$ to b was a factor of from 0.5 to 0.57, with dispersions in the range $\sigma = 0.15$ to 0.19. In studying Shull's results, the fractional reduction of b -value showed no apparent correlation with cloud EW. The large dispersions indicate that there is a significant random element in the fraction of $b_{Ly\alpha}$ that is due to bulk motions or clustered sub-condensations.

In Fig. 8, the derived b -values of clouds from the *FUSE* analysis are displayed as filled circles together with their $1-\sigma$ errors in W and b . The lower limit of their distribution should be limited by the thermal equilibrium, as the turbulent broadening approaches zero. A theoretical limit for the thermal broadening for lower EW clouds can also be applied by noting the column-weighted temperatures of model absorption systems, as discussed in §5.2.2, and plotted as open pentagons in the figure. The apparent linear trend of the latter three points is extended (dashed line) to high EW. It is seen that the derived b -values of large EW clouds obey the lower-limit that thermal broadening in absence of turbulence would imply. The equation of the line is,

$$b = 11 + 0.04375 W \text{ km s}^{-1}. \quad (31)$$

Also shown in Fig. 8 are the cloud data of Penton et al. (2000a), which have been reduced to 55% of their recorded $b_{Ly\alpha}$ values, in anticipation of the applicability of a similar correction factor for lower EW clouds (see §8). The appearance of a few clouds below the line of thermal broadening limit should not alarm the reader; in applying the mean reduction factor, we are introducing an error of order 30%; the fractional dispersion in the relation of b to $b_{Ly\alpha}$ from the Shull et al. (2000) data. For a cloud of true b -value 15 km s^{-1} , the $1-\sigma$ error is of order 4.5 km s^{-1} , enough to displace a cloud with small bulk motions to well-below the line.

Figure 8 demonstrates that b -values of clouds can be characterized as having a clear minimum for a given EW. Clearly, though, this will over-estimate the column density

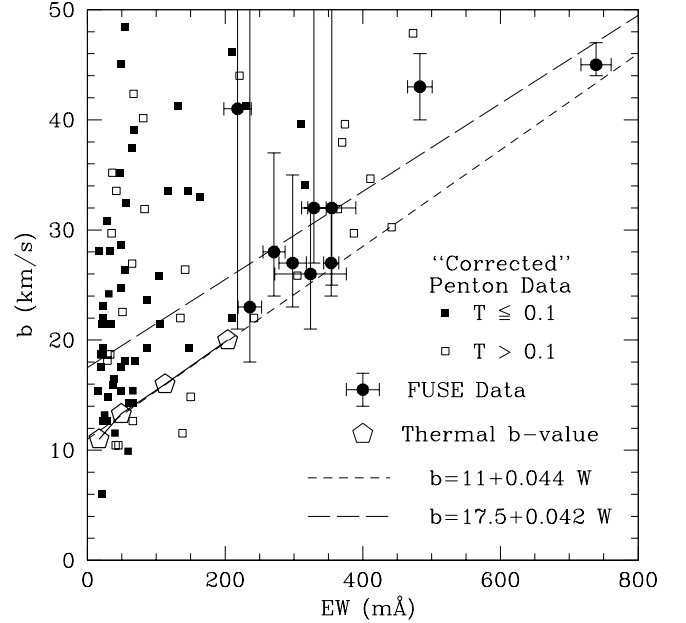


FIG. 8.— The b -value data of Shull et al. (2000) using *FUSE* (large solid circles with error bars), plotted against the rest EW. These results imply that intrinsic b -values for clouds with $W \geq 200$ mÅ are roughly half of the observed $b_{Ly\alpha}$ (see §5.3). The cloud data are presented as small squares; larger tidal fields ($\mathcal{T} \geq 0.1$) are open squares, and for $\mathcal{T} \leq 0.1$, solid squares. These Doppler parameters have been reduced to 55% of their $b_{Ly\alpha}$ value, according to this prescription. Open pentagons represent a theoretical lower limit to the observed b -value, based on the column density-weighted temperature of the model clouds for log-columns of 12.5, 13.0, 13.5, and 14.0, left to right (see §5.3). The short-dashed line is an extension of the trend of the pentagons, showing that the *FUSE* data obeys the envelope. The long-dashed line represents the approximate median relationship (see text). See text for details.

of an average cloud. However, a median b -value line may be drawn (long-dashed line) as a function of EW that is more relevant for transforming the EWDF to the CDS since it approximates the most probable b -values. This line has the equation

$$b \approx 17.5 + 0.042 W \text{ km s}^{-1}, \quad (32)$$

and is designed to represent the contributions of thermal broadening as well as bulk motions or the effects of unresolved components.

The result of applying these formulaic relations to the clouds via Eq. 29 results in the mean, and void EWDFs (Fig. 1) being transformed into a CDS. This is shown in Fig. 9, where the dotted lines represent the results of applying Eq. 31 to void, and mean cloud catalogs, and the solid lines represents the application of Eq. 32. The dashed lines accompanying these plots represent the CDS that would result from an untruncated isothermal sphere ($\vartheta = 2$, resulting in a spectral slope $\mathcal{S} \simeq -0.67$ top line), and a truncated isothermal sphere (lower dashed line), where the truncation radius scales with $r_t \simeq 144 h_{75}^{-1} \text{ kpc}$ for a cloud circular velocity $v_c = 21 \text{ km s}^{-1}$, about twice the scaled truncation radius assumed in Paper 1 (where $R_t = 500 X_v h_{75}^{-1} \text{ kpc}$). At this distance the overdensity of baryons and DM (assuming baryons follow DM) is $2.57 \Omega_b \rho_{crit}$, and thus shows the strong effect of a trun-

cation (such as from ram pressure stripping of diffuse, dissipated gas in filaments) on the CDS slope at low N_{HI} .

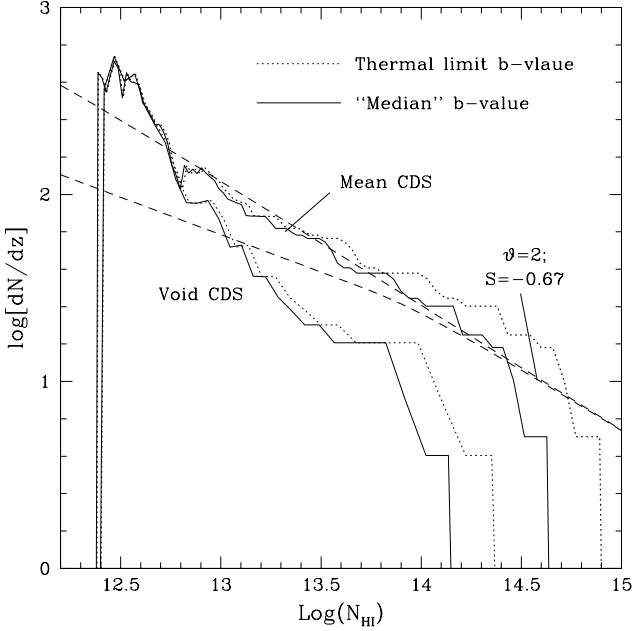


FIG. 9.— The observed column density spectrum derived using Eq. 31 (dotted lines), and Eq. 32 (solid lines), for the volume-weighted column density distribution (upper pair of lines) and the void CDS ($\mathcal{T} \leq 0.03$, lower pair). These distributions are compared to an analytic fit of arbitrary normalization for an untruncated isothermal baryon distribution (upper dashed line) and a truncated isothermal model with $r_t \simeq 144$ kpc for a halo with $v_c \simeq 21$ km s $^{-1}$ (lower dashed line). The effect of truncation is to diminish the number of low column density absorbers. The slope of the untruncated line is $S = -0.67$.

For the purposes of transforming an EWDF into a CDS, or vice versa the median relationship of $b(\mathcal{W})$ (Eq. 32) will henceforth be used. Though the error at column densities $N_{HI} \gtrsim 10^{13.5}$ cm $^{-2}$ may be substantial, smaller columns will be minimally affected, as can be seen in Fig. 9.

6. MODELING DISTRIBUTIONS OF SUBGALACTIC HALOS

The foregoing developments now enable the modeling of the CDS with distributions of model clouds. Cloud profiles can be combined into a column density spectrum, given a distribution of halo velocities. The primary method of determining the halo distribution function used here involves transforming the luminosity function (LF) into a halo velocity distribution function (hereafter HVDF). Additional useful information can be garnered by comparing our results to those emerging from numerical simulations.

The required procedure can be outlined as follows: First, extract the column density of a model cloud as a function of projected radius from a $z = 0$ product of the 1-D simulation. Secondly, combine this with a distribution of halos, and compare this synthetic spectrum to observations.

Since clouds are here assumed to be sub-galactic perturbations, I approach the subject by transforming the LF of galaxies into a HVDF that can be used to synthesize a CDS out of model clouds. The halo mass and velocity distribution functions of galaxies are determined by applying the Tully-Fisher (TF) relation to the galaxy luminosity function.

The TF relation be used to transform the luminosity function into an HVDF. It can be represented in many ways. Perhaps the simplest is as the power-law,

$$\frac{\mathcal{L}}{\mathcal{L}^*} = \left(\frac{v_c}{v_c^*} \right)^\beta, \quad (33)$$

where $v_c^* = 161$ km s $^{-1}$ (see §5.1 of Paper 1). The value of the constant β is a function of the photometric band being used. For the B -band, $\beta = 2.91$, and for the K -band, $\beta = 3.51$ (Tully & Pierce, 2000). Note that all symbols with a star, *e.g.*, M^* , R_t^* , & etc., refer to expectation values for an \mathcal{L}^* system, itself referring to the point of inflection of the Schechter form of the LF (*i.e.*, the “knee”).

As long as there is a calibrated TF relation corresponding to (*i.e.*, in the same spectral bandpass as) a given LF, one may apply a transformation of the LF into a mass, or velocity-DF. Below, is detailed the application of this transformation.

6.1. Transforming the LF to a Velocity or Mass DF

The halo velocity or mass distributions are based on the luminosity function. For these distribution functions I make the following syntactical simplifications,

$$\begin{aligned} X_{\mathcal{L}} &= \frac{\mathcal{L}}{\mathcal{L}^*}, \\ X_v &= \frac{v_c}{v_c^*}, \\ X_{\mathcal{M}} &= \frac{\mathcal{M}}{\mathcal{M}^*}, \end{aligned} \quad (34)$$

where \mathcal{M} represents the halo mass. The Schechter luminosity function is,

$$\phi_{\mathcal{L}} = \phi_{\mathcal{L}}^* X_{\mathcal{L}}^\alpha e^{-X_{\mathcal{L}}}, \quad (35)$$

(Schechter, 1976) and is a differential DF. A 1-D analogue to the Jacobian will transform the LF into something else. For instance, to transform a Schechter distribution $\phi_{\mathcal{L}}$ into a HVDF (ϕ_v) we have, $\phi_v = \phi_{\mathcal{L}} \partial X_{\mathcal{L}} / \partial X_v$. Partial derivatives are calculated from the following scaling relations for a truncated ISOT halo (see Paper 1, Eq. 29),

$$X_v = \frac{R_t}{R_t^*} = X_{\mathcal{L}}^{1/\beta} = X_{\mathcal{M}}^{1/3}, \quad (36)$$

where R_t is the galaxy halo truncation radius. The truncation radius utilized here, for clouds as well as galaxies, is such that the total mass density at R_t is $\rho(R_t) = 10 \rho_{crit}$. For the NFW halo the following scaling relations obtain (Paper 1, Eq. 40),

$$X_v = \left(\frac{R_{max}}{R_{max}^*} \right)^{0.67} = \left(\frac{R_{vir}}{R_{vir}^*} \right)^{0.76} = X_{\mathcal{L}}^{1/\beta} = X_{\mathcal{M}}^{0.30}. \quad (37)$$

As with Paper 1, we correct both the ISOT and NFW halos for the amount of baryons expected to be associated with it according to the assumed value of Ω_b/Ω_m . With baryons included, $v_c^* = 161.5$ km s $^{-1}$ (see §5.1.1 of Paper 1), but the dark halo has a halo $v_c^* = 144$ km s $^{-1}$.

Since $X_{\mathcal{L}} = X_v^\beta$ (Eq. 33),

$$\phi_v = \phi_{\mathcal{L}} \frac{\partial X_{\mathcal{L}}}{\partial X_v} = \beta \phi_{\mathcal{L}}^* X_v^{\beta(\alpha+1)-1} e^{-X_v^\beta}. \quad (38)$$

This halo velocity distribution function is identical for ISOT and NFW halos. The mass function for the ISOT halo is,

$$\phi_{\mathcal{M}} = \phi_{\mathcal{L}} \frac{\partial X_{\mathcal{L}}}{\partial X_{\mathcal{M}}} = \left(\frac{\beta \phi_{\mathcal{L}}^*}{3} \right) X_{\mathcal{M}}^{\beta(\alpha+1)/3-1} e^{-X_{\mathcal{M}}^{\beta/3}}, \quad (39)$$

while for the NFW halo we have,

$$\phi_{\mathcal{M}} = \phi_{\mathcal{L}} \frac{\partial X_{\mathcal{L}}}{\partial X_{\mathcal{M}}} = (0.3\beta \phi_{\mathcal{L}}^*) X_{\mathcal{M}}^{0.3\beta(\alpha+1)-1} e^{-X_{\mathcal{M}}^{0.3\beta}}, \quad (40)$$

Note that the exponential may be safely ignored for clouds, that have X_v and $X_{\mathcal{M}} \ll 1$.

The normalizations for each of these distributions can easily be calculated using the normalizations of the luminosity function. For the B-band LF, it is thought wise to interpolate the bracketing Sloan Digital Sky Survey (SDSS) normalizations to the B-band owing to the apparent consistency of their normalizations (see Appendix of Paper 1) and the large database used. We therefore use,

$$\phi_B^* = 0.022 \text{ h}^3 \text{ Mpc}^{-3} = 0.0093 \text{ h}_{75}^3 \text{ Mpc}^{-3}. \quad (41)$$

The distribution functions given in this section provide the basic framework for placing our halos into the universe. Although there are some conflicting indicators of which value of the slope α to apply, we may either prevail upon the criterion that α should be steep enough to explain the void cloud line density, or find a preferred value for α based on other compelling work.

6.2. Comparison with Previous HVDF Simulations

Cosmological simulations of hierarchical clustering (*e.g.*, Klypin et al., 1999; Klypin, 2002) (hereafter K99, and K02, respectively) provide the basis for deriving velocity and mass distribution functions of halos. How do the slopes of these distributions relate to the functional forms derived above? K02 noted an environmental dependency in the halo velocity distribution, with slopes -3.1 in groups, and -4.0 for isolated halos. With these facts we can find the Schechter faint-end slope parameter α that is consistent with these values. For small halo velocities, the HVDF (Eq. 38) can be simplified by removing the exponential which is ~ 1 for cloud halos. The HVDF is the same for ISOT and NFW, but there are two different environments; the dense (*i.e.*, group), and the isolated environments. I alternately equate the HVDF slope, $\beta(\alpha+1)-1$, to -3.1 , and -4.0 , and derive the slope parameter using $\beta_B = 2.91$: $\alpha = -1.72$, and -2.03 , for group, and isolated halo distributions, respectively. Note that these simulations presume NFW halos. It stands to reason that the isolated halo distribution would be more applicable to void cloud distributions.

By equating the mass function slopes in Eqs. 39 and 40 (excised of their exponentials) to that of the differential mass function with a slope of -1.8 , as found by K02, I find, $\alpha = -1.83$ and -1.93 , for ISOT, and NFW, respectively ($\beta_B = 2.91$). These represent values a mixture of isolated and group halos.

If isolated NFW halos have a slope parameter $\alpha = -2.03$, perhaps the slope parameter for isolated ISOT halos can be estimated by the difference between

ISOT and NFW slopes for mixed environments ($\alpha = -1.83$ and -1.93 , respectively, as above). Since the ISOT slope was flatter than the NFW mass function by 0.1 for mixed environments, then this would imply that for isolated ISOT halos, $\alpha = -2.03 + 0.1 \simeq -1.93$. I consider a slightly rounded value $\alpha = -1.95$ to be a provisional order-of-magnitude prediction for ISOT clouds in voids.

This steep slope, in comparison to a faint-end slope of $\alpha \approx -1.25$ for galaxies (Blanton et al., 2001), demonstrates the source of the “missing galactic satellites” problem (*e.g.*, K99). The suggestion of K99 is that the missing satellites may be clouds, rather than dwarf galaxies. In this case, their work may imply that the parameter α , if it is taken as referring to the demographics of halos in general, rather than the luminosity of halos, may be indicative of the presence of numerous small halos that are not luminous. Whether these are LSB galaxies, HVCs or Ly α clouds, a steep EWDF slope parameter suggests that a significant amount of mass may be tied up either in small halos, or in an unconsolidated component, as we shall see in §6.6.

6.3. Assembling the CDS

The column density spectrum is calculated from model clouds according to the equation,

$$\frac{dN(\geq N_{HI})}{dz} = \frac{c}{H_0} \sum_{n=0}^{13} \phi(X_v(n)) \pi r_{N_{HI}}^2 \delta X_v(n), \quad (42)$$

where $\phi(v_c)$ is given by Eq. 38, $r_{N_{HI}}$ is the radius at which a column density N_{HI} is detected, $X_v(n)$ is given by Eq. 28, and $\delta X_v(n)$ is the bin width. The cadence in X_v indicates that $\delta X_v = X_v(10^{0.025} - 10^{-0.025}) = 0.1152 X_v$. The radius at which a given column density can be observed in a cloud of a given v_c is determined by the method described in §5.2.1. The model column density spectra can then be compared with the observations.

The goal of modeling the distribution of clouds is to reproduce the observations. Not only must the line densities as a function of column density be matched, but it is also important to reproduce the shape of the CDS.

Equation 38 shows how the halo distribution function is calculated as a function of X_v , and demonstrates the role of the faint end slope α and the TF slope β in determining the low-velocity end of the HVDF. Since it is theorized that the distribution of sub-galactic halos is in continuity with the galaxy halo EWDF, the normalization of the galaxy luminosity function in voids will be a good place to start the modeling; the modeled distribution of halos must be based on a normalization $\phi^*(void)$. It has been suggested that galaxies are present in voids at $\sim 1/10$ the average density (El-Ad & Piran, 1997, 2000). A somewhat larger galaxy density is found in Boötes (Dey et al., 1995; Cruzen et al., 2002). An upper-limit of current thinking might be represented by the simulations of Cen & Ostriker (1999), which assumes that $\Omega_m = 0.4$ and estimates that $\Omega_V/\Omega_m \simeq 0.26$, consistent, perhaps, with roughly an equal mass in clouds and in galaxies. A low normalization would seem to imply a low total void density, yet since the spectral slope of the void cloud HVDF may be steep, this is not necessarily inconsistent with a large density. Therefore, I provisionally adopt the normalization,

$\phi^*(\text{void}) = 0.1\phi^* = 9.3 \times 10^{-4} h_{75}^{-3} \text{ Mpc}^3$ (see Eq. 41), with hopes that it can explain the data.

The somewhat arduous transformation of the TF relation to an HVDF, and the number of parameters that need to be evaluated, may give the impression that there are many free parameters utilized in this analysis. This is a misconception, for none of the parameters are given arbitrary values. The slope parameter α is reasonably constrained by the modified Press-Schechter simulations of K02 (see §6.2), the TF slope β is constrained by the B-band TF relation, which has a well-known value (Tully & Pierce, 2000), and the normalization of the void EWDF is observationally constrained, as noted above. Of these, the latter would seem to have the greatest range of uncertainty, and is the only parameter used as though it were a truly free parameter. However, none of the values of these parameters are arbitrary, or disconnected from observations.

The effects of using various slope parameters α on the derived CDS are discussed in the following section.

6.4. The model CDS with slope parameter α

A constant slope parameter α is the most obvious beginning point for investigating the relationships between our parameters and the product CDS.

6.4.1. The ISOT model

I first consider the ISOT model. Recall that with the ISOT halo, clouds with large v_c significantly restrain the expansion of baryons from the dark halo (§5.1.1). As a result, columns $N_{HI} \gtrsim 10^{12.4} \text{ cm}^{-2}$ are detected for the velocity range $10 \leq v_c \leq 25 \text{ km s}^{-1}$. Figure 10 displays model CDS (solid curves) for various slope parameters α using the above normalization and the ISOT model profiles (Fig. 6). When applying slopes of $\alpha = -1.0$ or -1.4 , low line densities result. If the slope is -1.4 , then the normalization will have to be increased by a factor of 30 in order to give rough agreement with the observed line density, making the normalization in void space greater than the average by a factor of 3, which is absurd. When $\alpha \approx -1.95$, as suggested in §6.2, the resulting modeled line density is comparable to the observed value. In order to fit the low column density end of the CDS, a slope parameter of order $\alpha \approx -3.5$ is required (dotted line in Fig. 10). However, integrating over the HVDF (for details, see §6.6), the total mass density for clouds $5 \leq v_c \leq 25 \text{ km s}^{-1}$ is $\Omega_{cl} \gtrsim 0.028$, of order 10% of the assumed mean density $\Omega_m = 0.3$, when the truncation radius is taken to be $r_t = 500 X_v h_{75}^{-1} \text{ kpc}$, where X_v is given by Eq. 36, as was the standard with Paper 1 (§5.1.1). When systems of velocity $10 \leq v_c \leq 150 \text{ km s}^{-1}$ are used, then $\Omega_V = 0.09$, and $\Omega_V/\Omega_m \simeq 0.3$. The truncation radius is such that the density at r_t is about 10 times the critical. Considering that the rest of void space is unlikely to be absolutely empty, this value for Ω_V must be a lower limit.

6.4.2. The NFW model

NFW halos do not produce any absorbers with $N_{HI} \geq 10^{12.4} \text{ cm}^{-2}$ in the range $10 \leq v_c \leq 22.4 \text{ km s}^{-1}$; the next higher velocity bin ($n = 13$ in Eq. 20) experiences collapse in the center, presumably forming stars. The line density, even at $N_{HI} = 10^{12.2} \text{ cm}^{-2}$ is less than one cloud

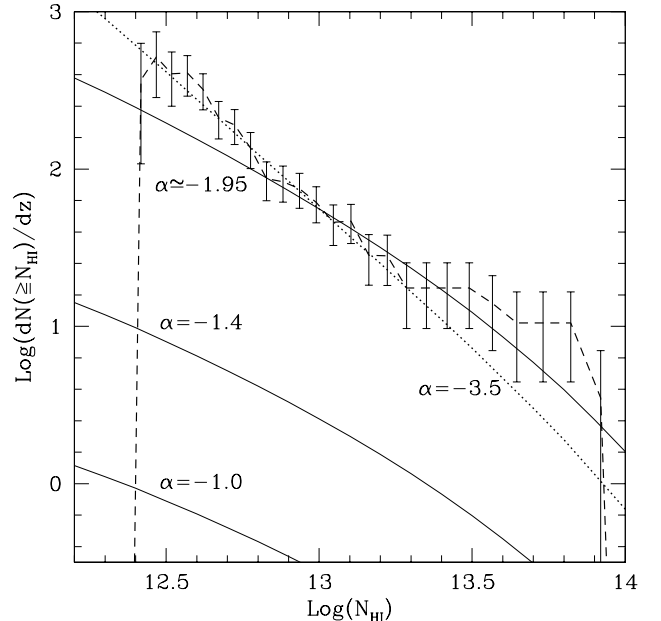


FIG. 10.— A comparison of the observed void column density spectrum for low- z clouds ($\mathcal{T} \leq 0.1$) (short-dashed line) with spectra that would result from a HVDF resulting from an extension of the SLF faint-end slope $\alpha = -1.0$, -1.4 , and -1.95 , normalized at $0.1\phi^*$ (solid lines). To fit the slope at $N_{HI} \lesssim 10^{13.3} \text{ cm}^{-2}$, an HVDF with a slope parameter $\alpha \simeq -3.5$ is required (dotted line), though the required normalization is an order of magnitude lower than $0.1\phi^*$.

per unit redshift for parameters that produce an acceptable fit with ISOT halos. The reasons for this shortfall are two-fold. First, NFW halos are about 5 times less massive than an ISOT halo of the same v_c , and hence, have 5 times fewer baryons. Second, the lower mass of the halos cannot as effectively slow the baryonic outflow and dispersal as can the ISOT model; the trend of the restraint of the outflowing gas for large v_c , noted in the inset of Fig. 6, is not apparent in the NFW profiles (Fig. 7). Further, comparison of Figs 6 and 7 shows that the central baryonic densities of NFW halos are of order 1/10 of an ISOT halo at comparable halo velocities. Since no absorption systems are produced, this halo model fails to explain the observed EWDF, and I forego any further consideration of it.

6.5. The Shape of the CDS

In this section I take a critical look at the observed CDS to see what degree of confidence is justified in its slope at the low, or “high” column density end ($\sim 10^{14} \text{ cm}^{-2}$). Figure 10 shows the Poisson error bars for data at $z \leq 0.036$ (see §6.2.1 of Paper 1). Adjacent error bars are not independent of each other since the same clouds may contribute to a range of EWs. When data from all redshifts are used, the Poisson errors are smaller, but the slope at the low column-density end ($W \lesssim 40 \text{ mÅ}$, or $N_{HI} \lesssim 10^{13.3} \text{ cm}^{-2}$) is moderately flatter than if only data from $z \leq 0.036$ is used (see Fig. 11 and 12 of Paper 1). This is probably attributable to an underestimation of the tidal field at higher redshifts, with consequent contamination of void catalogs with non-void clouds, all

occasioned by the probable non-detection of less-luminous galaxies in the proximity of the clouds. I conclude that the steepness of the slope apparent at $\log(N_{HI}) \lesssim 13.3$ in Fig. 10 is highly significant, though what it means is yet to be determined (see §6.6).

However, the “bump” in the CDS at columns $N_{HI} \gtrsim 10^{13.5} \text{ cm}^{-2}$, remains essentially unchanged when higher redshift data are excluded. Is this a real feature? There are five clouds with $N_{HI} \geq 100 \text{ mÅ}$ (which, using Eqs. 32 and 29, implies $N_{HI} \gtrsim 10^{13.35} \text{ cm}^{-2}$) contributing to this end of the low- z void distribution ($\mathcal{T} \leq 0.1$), as opposed to $n_{cl} \sim 20$ at $N_{HI} \lesssim 10^{12.9} \text{ cm}^{-2}$. It is helpful, at this point, to take a detailed look at the five clouds with $\mathcal{W} \gtrsim 100 \text{ mÅ}$ in the low- z data with the help of a program that assesses the prospects for the physical association of clouds (*i.e.*, gravitationally bound) with galaxies on the basis of the galaxy absolute magnitude (mass is derived assuming the more massive ISOT halo), the relative velocity of cloud and galaxy, and the projected radius, (Manning, in preparation). The galaxies considered for this routine are those within 750 km s^{-1} of the cloud in question if the projected radius $r_p \leq 2 \text{ Mpc}$, or within 350 km s^{-1} if outside this.

Two of the five low- z clouds have derived local tidal fields of $\mathcal{T} = 0.073$ and 0.098 . Both are found to have one sub- \mathcal{L}^* galaxy at a projected distance $r_p > 2 \text{ Mpc}$, with cloud-galaxy LOS relative velocities of 66 and 72 km s^{-1} , respectively, for which the program predicts probabilities of physical association of $\sim 13\%$, and 4% , respectively. These clouds can be found in Fig. 4 of Paper 1 in the sightlines to MRK 335 (Fig. 4k, 1241.09 Å) and AKN 120 (Fig. 4h, 1247.94 Å), respectively. But even this possible physical association could not produce a significant peculiar velocity along the LOS because of the large projected distance to the galaxy, and hence the attributed tide cannot be far wrong. Of the other three, two have tidal fields $\mathcal{T} \approx 1 \times 10^{-3}$, and have no galaxies within the search area. The other, with $\mathcal{T} \simeq 7 \times 10^{-3}$, has a late-type sub- \mathcal{L}^* galaxy at a projected radius $r_p \simeq 430 \text{ kpc}$ (the CfA Redshift Catalog, Huchra et al. 1990, Huchra, Geller, & Corwin 1995, Marzke, Huchra, & Geller 1996, Grogin, Geller, & Huchra 1998, Huchra, Vogele, & Geller 1999)⁵, but at a relative velocity of $\Delta v \simeq 350 \text{ km s}^{-1}$. The probability of association was rated at $\sim 4\%$. The galaxy velocity error was listed as $\delta v = 1 \text{ km s}^{-1}$, and the cloud redshift error from Penton et al. (2000a) was listed as $\delta v = 6 \text{ km s}^{-1}$. Thus, these five clouds have few prospects for a physical association in which significant peculiar velocities from gravitational interactions could result, and fewer chances for associations that would give significant LOS peculiar velocities. With high confidence, I claim these 5 clouds are truly remote, and are not anomalously present in void catalogs.

It is noteworthy that the void filling factor at $\mathcal{T} \lesssim 0.01$ is ≈ 0.44 (see Fig. 7, Paper 1), while at $\mathcal{T} \lesssim 0.1$, $f_V \simeq 0.86$. Thus the volume in which the three low \mathcal{T} clouds appear is almost exactly the same as the volume in which the two at $0.01 \leq \mathcal{T} \leq 0.1$ clouds appear, making it seem likely that large clouds may be more prevalent in deep voids than in the void periphery. But the statistics are small, and we would be wise to seek more data before forming a

conclusion.

A possible explanation for those clouds that produce the excess above the model at $N_{HI} \approx 10^{13.7}$ (see Fig. 10) is that there exist clouds/proto-galaxies in voids with halo velocities $v_c > 25 \text{ km s}^{-1}$, for the analysis of the CDS of individual clouds shows that the larger the circular velocity of a cloud, the flatter the slope of the CDS that it produces; such additions would produce more absorbers at $\log N_{HI} \sim 13$ to $14 \text{ (cm}^{-2}\text{)}$. This can be understood by noting that the more massive the cloud, the more strongly it will hold its baryons, producing a steep density gradient at the edge, and resulting in a flat CDS (*cf.* Eqs. 16 and 17).

Recall that the gas in larger halos ($v_c \geq 25 \text{ km s}^{-1}$) collapse and produce stars in the 1-D simulations. However, if clouds have grown from hierarchical merging during their evolution, they would have been smaller during the early, high-density stages of evolution, achieving their larger size only recently. Because of the early evaporation of baryons from their core region, there might not be sufficient baryonic mass in the core to produce the cooling needed to trigger star formation. Therefore, with growing halos, the limiting circular velocity (as measured at $z = 0$) for SF is probably higher than 25 km s^{-1} .

But before pursuing this line of thought, it is important to consider the repercussions of taking literally the significant steep CDS slope at $N_{HI} \lesssim 10^{13.3} \text{ cm}^{-2}$ noted above.

6.6. Total mass distribution and slope parameter α

As noted in §6.4.1, the low column density end of the void CDS can be well-fit by an HVDF with a very steep slope parameter $\alpha \approx -3.5$. In this section I inspect the physical repercussions of this. As argued in §6.2, the HVDF may be simplified by removing the exponential (Eq. 35) when $X_v \ll 1$. Consider logarithmic bins of v_c such as was used in the simulations here; construct the bins such that each bin has a width $\delta X_v \equiv X_v \delta v_0 / v_0$, where $\delta v_0 / v_0 \ll 1$ is some appropriate constant. Then from Eq. 38, the number density of systems within a bin is,

$$\delta n_{bin} = \phi_v^* X_v^{\{\beta(\alpha+1)-1\}} X_v \left\{ \frac{\delta v_0}{v_0} \right\}. \quad (43)$$

Thus, the comoving number density per bin scales as

$$\delta n_{bin} \propto X_v^{\beta(\alpha+1)}. \quad (44)$$

When $\alpha = -1$, each logarithmic bin has an equal number of systems in it. However, when we consider the mass in each bin, we must multiply the number density by the mass per object.

For the ISOT halo, the mass scales as $M \propto X_v^3$ (Eq. 36),

$$\delta M_{bin} \propto X_v^{\beta(\alpha+1)+3} \propto X_{\mathcal{M}}^{\beta(\alpha+1)/3+1}, \quad (45)$$

that has equal masses in logarithmic bins when $\alpha = -(1 + 3/\beta) \simeq -2.03$ for $\beta_B = 2.91$. For this value of α , the mass function is flat in logarithmic bins.

For the NFW halo, virial mass $M_{200} \propto v_{max}^{3.30}$ (Eq. 37). The NFW bin mass is a somewhat different relation,

$$\delta M_{bin} \propto X_v^{(\beta)(\alpha+1)+3.3}, \quad (46)$$

⁵see <http://cfa-www.harvard.edu/~huchra/>

that has equal masses in logarithmic bins when $\alpha = -3.3/\beta - 1 \simeq -2.13$ for the same β_B .

Recall that a CDS formed using ISOT cloud profiles and a HVDF with $\alpha = -3.5$ would have an increasing mass in bins of progressively smaller velocity v_c , implying a divergence of the integrated mass. The sobering implications of this fact are softened, however, if sub-clustering is occurring. Further, it is reasonable that sub-halos should form in the flanks of larger halos, for the time-scale for collapse of perturbations is proportional to the inverse square root of the density, making it more likely for them to form there than in the regions between clouds. Thus, many of the small clouds that are detected in the CDS may not be independent, isolated clouds, but loosely associated with larger clouds. Since they are fashioned out of the stuff of the main cloud, they are not taken to add to its mass, unless such sub-halos are found to lie outside the truncation radius R_t . If sub-condensations exist, then accretion or hierarchical agglomeration is a distinct possibility in the halos of H I clouds in voids.

7. EXTENDING MODEL CLOUDS TO HIGHER V_C

Up to this point, the halos that have been used were fixed at $z = 6.5$. Such halos remained star-free only up to circular velocities of only up to $v_c \approx 25 \text{ km s}^{-1}$ (§5). However, the steep spectral slope of the void CDS at low column density appeared to require the presence of sub-clustered halos, since otherwise the indicative mass function would diverge. Likewise, it is difficult to reconcile the existence of CHVCs (Braun & Burton, 2000) with H I mass approaching $10^7 M_\odot$ (de Heij et al., 2002), with model clouds having maximum H I masses only $\lesssim 10^6 M_\odot$.

The behavior of the observed CDS relative to model CDS thus suggests the possibility of continued accretion and halo growth during the period from $z = 6.5$ to the present; that sub-halos cluster about larger halos implies that the circular velocities of clouds could grow by the accretion of those halos; their growth would explain the presence of CHVCs⁶ with H I masses approaching $10^7 M_\odot$. Figure 11, shows H I mass for fixed halos (open circles), corresponding to each circular velocity bin). The trend of fixed halos shown in Fig. 11, halos of velocity $v_c \gtrsim 40 \text{ km s}^{-1}$ could reach this H I mass.

Recall, however, that attempts to run models of such large halo velocities failed for fixed halos, because the central baryonic core, thought to roughly follow the dark matter before reionization, was not able to support itself, as described in §5. However, if halos are slowly “grown”, such as by accretion, then larger halo velocities at $z = 0$ may be attainable without these indications of star formation, with H I masses more in line with observations of CHVCs may be attained.

In what follows, I adopt this model of accretion. A rough approximation of that growth rate was made by assuming that the largest fixed cloud that escapes collapse into star formation, could grow to the largest cloud which today has an H I mass of $10^7 M_\odot$, as asserted by Braun et al. (2002). The circular velocity of that halo was approximated by connecting the trend in H I mass with fixed-halo circular

⁶the optical surface brightness of local CHVCs is constrained to be $\lesssim 10\%$ of the faintest Local Group dSph (L. Blitz, private communication 2002)

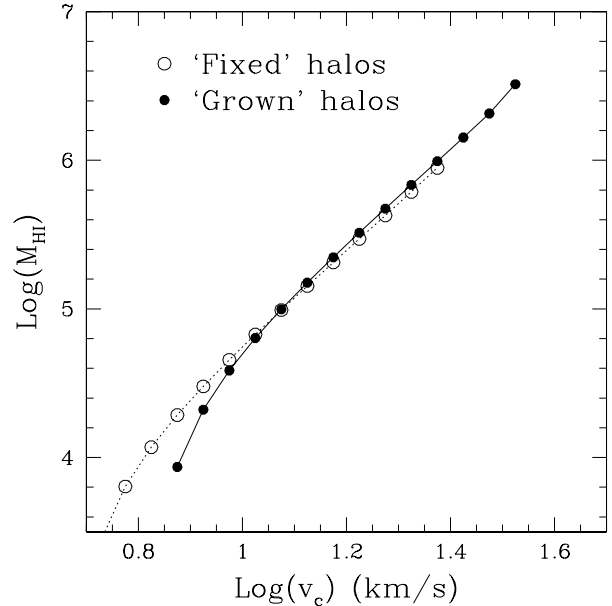


FIG. 11.— The H I mass in terms of the circular velocity for clouds that grow according to Eq. 47 (filled circles and solid line) compared to that of the fixed halo (open circles, dotted line). The logarithm of the H I mass is shown as a function of the logarithm of the cloud circular velocity (solid line) for untruncated clouds.

velocity to the maximum cloud H I mass of $10^7 M_\odot$ (see Fig. 11).

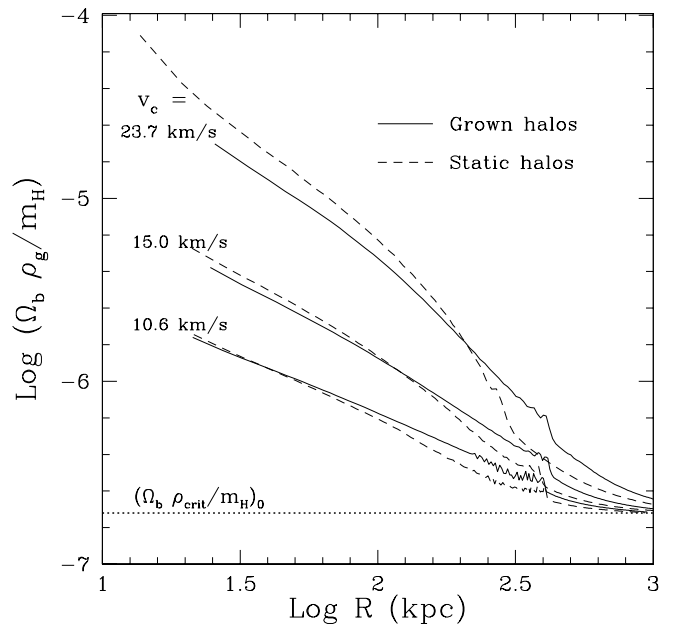


FIG. 12.— Density profiles for clouds with circular velocity $v_c \approx 9.4, 15.0$, and 23.7 km s^{-1} for fixed halos (dashed lines) and for halos which grow according to Eq. 47 (solid lines). The more power-law like profile results in a steeper CDS slope (see Fig. 13).

The clouds are “grown” gradually, that is, by inserting increments of mass into the Lagrangian bins at each time

step in a way that mimics the equation,

$$v_c(t) = v_c(0) e^{k_a t}, \quad (47)$$

where $v_c(0)$ is the circular velocity at $z = 6.5$, the accretion constant $k_a \approx 0.78$ in units of inverse Hubble times t_H^{-1} , and t is in units of t_H . As DM is gradually loaded into the DM bins, their physical extents are scaled-up to mimic the larger core-radius of larger clouds (see §5.1.1 of Paper 1 for scaling relations). Mass is added to the baryonic bins in the same way, however, the radial positions are not altered directly, but allowed to evolve according to the pressure gradients and total gravity of the cloud. This approximation may result in a slightly more concentrated distribution of baryons than if the gas was originally associated with the accreting sub-halos. But the inward migration of DM would tend to pull the gas inward anyway. It appears that the only significant difference between the model and the envisioned reality may be a weaker discontinuity in the model between the outflowing wave from the original ionization of the cloud and the infalling gas from the periphery. But the relatively mild difference between fixed halo, and grown halo evolution suggests that a thoroughly accurate treatment of this problem would present a final profile much like the grown halos.

Results for some of the halos are shown in Fig. 12, where the solid density profiles represent the “grown” halos, and the accompanying dashed lines represent fixed halos of the same circular velocity. In general, the resulting halos have a modestly lower central density and a modestly greater density outside the core. In this way, clouds with central bin velocities up to $v_c = 33.5 \text{ km s}^{-1}$ were generated with no central baryon collapse, three more velocity bins than with fixed halos. For still larger halos, however, the innermost bins collapse, indicating the plausible formation of stars. The bin with center 37.6 km s^{-1} collapsed at very low redshift, indicating the possibility of very young void galaxies forming from such clouds. Thus, the growth of void clouds could explain the existence of blue compact galaxies at voids edges (Pustil’nik et al., 1995), with halo circular velocities $v_c \gtrsim 35 \text{ km s}^{-1}$.

For a given normalization ϕ_V^* , extending the halos to larger circular velocities in this way results in a larger line density at a given column density. As a result, the best fit to the observed CDS requires lowering the normalization to $\phi_V^* \simeq 0.06 \phi^*$. The resulting CDS, using the grown halos with HVDF slope parameter $\alpha = -1.95$, is presented in Fig. 13 as the solid line; the dashed line represents the fixed halos with $\phi_V^* = 0.1 \phi^*$. Note that the quality of the fit is greatly improved at large column densities. The excess at small column density is still expected, due to the sub-clustering of small halos in the flanks of major clouds. Modeling this component requires semi-analytic work beyond the scope of the present paper, and is deferred.

If the mass function is integrated over the range of model halo velocities which are detectable, the mass density in voids is, $\Omega_V \geq 0.022$, for $\phi_V^* = 0.06 \phi^*$ and $R_t = 500 X_v \text{ kpc}$. This is 78% of the mass density for fixed halos. The reason for this difference is first, the lower normalization, but this is partially compensated by the larger halos which emerge from the grown halo models.

8. DOPPLER PARAMETERS OF MODEL ABSORBERS

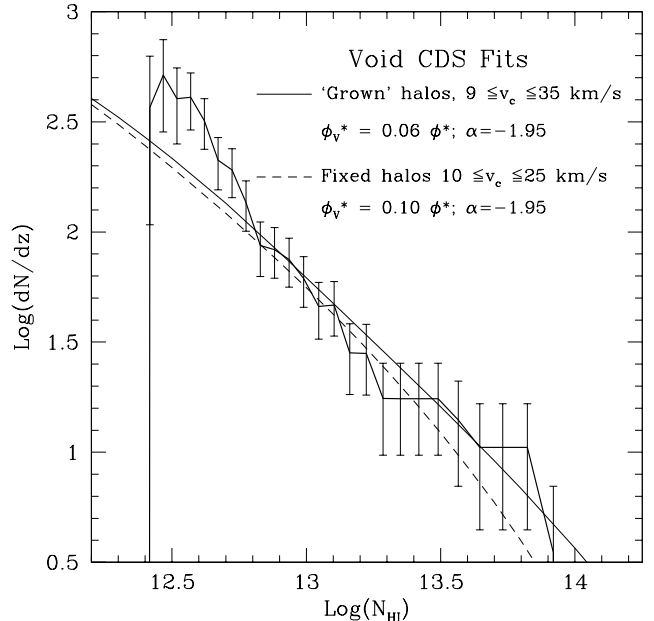


FIG. 13.— Predicted CDS using an HVDF with slope parameter $\alpha = -1.95$ for clouds evolved with fixed halos (dashed line), compared with halos which grow according to Eq. 47. The latter halos are detectable in 4 more bins than the former, one centered at 9.4 km/s, and three at 26.6, 29.9 and 33.5 km/s. The normalization for the grown clouds was $\phi_V^* = 0.06 \phi^*$, and for fixed halos, $\phi_V^* = 0.1 \phi^*$.

Recall that the diffuse absorbers expected from N-body simulations predict large Doppler parameters, and that this was one of the reasons that this author abandoned the diffuse cloud model (§1). The evolved baryon distributions pertinent to a given halo model have a wealth of detail in the program output of the 1-D simulations. This section investigates the Doppler parameters of the model absorbers. Fig. 14 shows the cumulative line density dN/dz contributed by each of the model halos, as normalized by $0.1 \phi^*$ for the fixed halos (panel a), and $0.06 \phi^*$ for grown halos (panel b); both with slope parameter $\alpha = -1.95$. Note that low column density absorbers are produced in a wide range of cloud models.

Figure 15 shows histograms of void (dotted) and non-void (solid lines) clouds for $\mathcal{W} \leq 50 \text{ mÅ}$ (panel a) and $\mathcal{W} > 50 \text{ mÅ}$ (panel b), for the low-redshift sample, $z \leq 0.036$. Panel a shows that low EW void clouds have remarkably uniform b -values, with a near-symmetrical profile with a maximum at $\sim 30 \text{ km s}^{-1}$, while panel b shows that of the higher EW clouds, non-void clouds predominate only at higher b -values. That is, almost half of the clouds with $\mathcal{W} \geq 50 \text{ mÅ}$ and $v_c \geq 40 \text{ km s}^{-1}$ are void clouds.

Fig. 14b shows that, for grown clouds, a cloud of column density $N_{HI} = 10^{12.4} \text{ cm}^{-2}$ can be produced by clouds of circular velocity $10.6 \lesssim v_c \lesssim 35 \text{ km s}^{-1}$. For purposes of illustration, I now undertake to closely inspect the thermal and velocity structure of model absorption lines produced by the extremes of halos producing this column density.

I estimate the core temperature of clouds with halo velocities $v_c = 10.6$ and 33.5 km s^{-1} using the method of §5.2.2. The smaller cloud is found to have a weighted temperature of 7863 K, while the larger cloud has a tem-

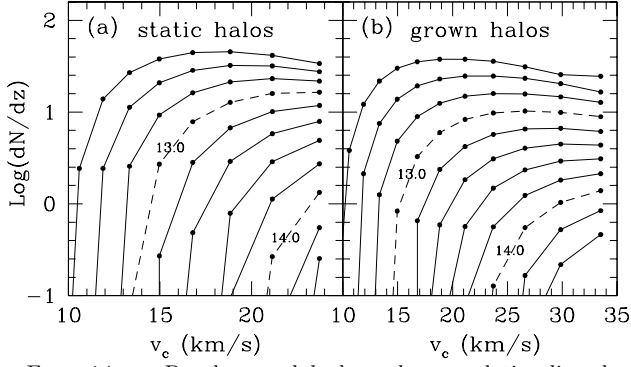


FIG. 14.— Panels *a* and *b* show the cumulative line density (greater than a given column density) as a function of the halo velocity bin for fixed, and grown halos, respectively. The top line is the minimum detected column density, $N_{HI} = 10^{12.4} \text{ cm}^{-2}$, with subsequent lines representing columns larger by 0.2 in $\log N_{HI}$. A few of the lines are labeled by the log of their column density. Low column density clouds are produced by clouds with a wide range of halo velocities.

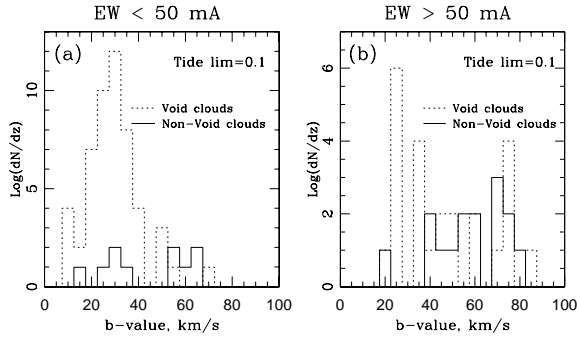


FIG. 15.— Cloud Doppler parameter histograms from Penton et al. (2000a) GHRs data for void (dotted) and non-void (solid line) catalogs (using $z \leq 0.036$), for clouds with $W < 50 \text{ mÅ}$ (left-hand plot), and $W > 50 \text{ mÅ}$ (right). For low-EW clouds there is a narrow range of b -values, while for larger clouds, b -values appears to vary over a wide range. Notice the difference in vertical scales between panels *a* and *b*.

perature of 5375 K. This can be understood by reference to Fig. 5, for the larger cloud has a much larger impact parameter than the smaller cloud ($r_p \simeq 500 \text{ kpc}$ versus $\sim 55 \text{ kpc}$, respectively), and hence has lower average densities.

There is apt to be large-scale turbulence in the clouds following reionization, especially toward the center where the density, and its gradient remain high, and the potential for convective instability is large. A plausible upper-limit for a cloud's turbulent velocity is the cloud virial velocity. The virial temperature is,

$$T_{vir} = \frac{1}{2} \frac{v_c^2 \mu m_H}{k_b}, \quad (48)$$

and may be converted to a virial b -value by $b_{vir} = \sqrt{0.0165 T_{vir}}$. The virial temperatures of the two clouds ($T_{vir} = 6776 \text{ K}$, and $67,756 \text{ K}$, for the smaller, and larger clouds, respectively) may contribute to the Doppler parameter. For the small 10.6 km s^{-1} cloud, the addition to b contributed by turbulence is apt to be small since the T_{vir} is less than the thermal temperature. For the large cloud, the turbulent component could dominate, depending on the impact parameter (hence column density). Since the

impact parameter of the large $N_{HI} = 10^{12.4} \text{ cm}^{-2}$ cloud is large, the sightline won't penetrate the virializing portion of the cloud ($r_p \lesssim 125 \text{ kpc}$). Instead, the velocity field of the expanding cloud may be an important addition. The LOS velocity difference within the FWHM of the line is found to be 25 km s^{-1} over the LOS distance, $l_{1/2} = 534 \text{ kpc}$, yielding $b_{vel} \simeq 15 \text{ km s}^{-1}$. If this material were in the Hubble flow, the FWHM velocity would have been $\sim 40 \text{ km s}^{-1}$, showing the physical effect of the negative peculiar velocities previously noted for large clouds (see Fig. 4).

The b -value associated with the smaller $N_{HI} = 10^{12.4} \text{ cm}^{-2}$ cloud is then $b = \sqrt{b_{therm}^2 + b_{turb}^2} \leq 15.5 \text{ km s}^{-1}$, where the b_{vel} component is ignored since it is found to be less than 2 km s^{-1} within the FWHM of the line. The direction of the inequality in the equation stems from the fact that v_{turb} is an upper limit for bulk motions in these absorbers. The lower limit is the thermal b -value; $b = 11.4 \text{ km s}^{-1}$. For the larger cloud, $b = \sqrt{b_{therm}^2 + b_{vel}^2} \geq 17.7 \text{ km s}^{-1}$, where the turbulent (virial) motions of the cloud have not been included since only the outer cloud is probed. This velocity is a lower limit because some turbulent motions are likely.

Larger clouds, such as $N_{HI} = 10^{13.5} \text{ cm}^{-2}$ ($W \simeq 130 \text{ mÅ}$), have averaged temperatures on order $\sim 16,900 \text{ K}$ ($b_{therm} = 16.7 \text{ km s}^{-1}$), produced by halos of velocity $17 \lesssim v_c \lesssim 33 \text{ km s}^{-1}$. They give total b -values $b \lesssim 24$ to $b \lesssim 37 \text{ km s}^{-1}$, where I have ignored the cloud expansion broadening, which is dwarfed by possible turbulent motions. The impact parameters for these systems, $120 \lesssim r_p \lesssim 180 \text{ h}_{75}^{-1} \text{ kpc}$, may probe virializing regions.

These values agree well with the range of b -values presented in (Davé & Tripp, 2001) (see their Fig. 6a).

In comparing the analysis of b -values in Davé & Tripp (2001) to those in this paper, it is interesting to note that though the former predict higher temperatures for a given gas density (see Fig. 5), the thermal b -values as a function of a given column density (Eq. 8) are smaller. Table 1 shows a compilation of thermal b -values; column 1 is the log column density; the next column shows the Davé & Tripp (2001) thermal b -values; third are those of the present study. It would appear that at the same column density, the former must have substantially lower H I densities (by a factor of ~ 3 to 5) than the discrete clouds considered here, and therefore have proportionately larger integration paths. The irony should not be missed; the absorbers of Davé & Tripp (2001) are supposed to occupy a dense environment, but are less dense than the void absorbers modeled in the present effort.

TABLE 1
PREDICTED THERMAL DOPPLER PARAMETERS

$\log N_{HI} (\text{cm}^{-2})$	$b_{therm} (\text{km s}^{-1})$ Davé & Tripp (2001)	$b_{therm} (\text{km s}^{-1})$ Manning
12.5	9.2	11.3
13.0	11.7	13.8
13.5	14.9	16.7
14.0	19.0	21.1

I have shown that centrally condensed clouds based on sub-galactic halos produce Doppler parameter distributions consistent with observed clouds (Davé & Tripp, 2001). Perhaps, however, good agreement is *not* expected since Davé & Tripp (2001) purport to study predominantly non-void clouds, while the present study models void clouds. On the other hand, if the lines of sight covered in their paper are like those in Penton et al. (2000a), then Fig. 14 would indicate that most clouds, especially those of lower column density, are in fact void clouds, and substantial agreement with the echelle observations would be expected.

However, it is unlikely that one could decide between giant sheets and discrete, sub-galactic absorbers on the basis of Doppler parameters alone. The conclusion to be taken away from this section is that discrete halos produce results that are consistent with observations of resolved Doppler parameters in low-redshift Ly α clouds.

9. SUMMARY

In the introduction, two possibly problematic aspects of recent N-body/hydro simulations were noted; first, the fact that Ly α absorbers are expected to be produced in diffuse clouds by a “fluctuating Gunn Peterson” effect (Croft et al., 1998; Davé & Tripp, 2001), rather than by absorption in discrete halos. Second, that low-redshift absorbers are expected in diffuse filamentary structures surrounding galaxy concentrations, but not in voids.

The analysis in §2 showed that indeed, diffuse structures could not provide an explanation for the void absorbers. The analysis in the balance of the paper showed that discrete halos may restrain the baryons from evaporating to a degree sufficient for absorption systems to be produced that are consistent with observations. This implies that it is *not* a good approximation to assume that small halos would not retain a significant quantity of their baryons following reionization.

However, the problem goes farther than just contesting the N-body Ly α cloud simulations. For the current halo paradigm, NFW, also fails to explain the absorbers since those halos small enough to escape star formation are not massive enough to hold baryons against photo-evaporation. In short, a more massive halo is needed.

I have shown that an isothermal halo *can* explain the absorbers, within the cosmological parameters investigated here. Some might argue that the ISOT halo is not physically realistic since they cannot be virialized. However, I am not proposing that “ISOT halos” are totally virialized. Instead, I propose (as noted in §4.1.4) that the isothermal density profile is a fair description only of the total mass distribution.

The NFW halo is said to be universal, but when applied to rich galaxy clusters, it fails to explain the mass distribution; analysis of galaxy-galaxy correlations by Seldner & Peebles (1977) showed that the distribution of galaxies ($n_{gal} \propto R^{-2.4}$) around rich clusters extends to 15 h $^{-1}$ Mpc, without a feature that would suggest the expected sharp decline in density beyond R_{max} (~ 0.8 Mpc), or at the virial radius (~ 2 Mpc). Recent results of McKay et al. (2002) substantiate this claim using isolated groups of galaxies. They find $n_{gal} \propto r^{-2.1}$, and a LOS velocity dispersion σ_r that shows no significant variation between apertures of 133 to 670 h $_{75}^{-1}$ kpc (whereas $r_{vir} \approx 250$ h $_{75}^{-1}$ kpc). These

results appear to support an isothermal mass distribution – either truncated at a very large radius, or untruncated.

Evolved ISOT baryon profiles whose halos were assumed to be un-evolving, were found to be more compact, and tended to form stars at velocities $v_c \gtrsim 25$ km s $^{-1}$, leaving a gap between the largest model clouds and smallest galaxies and CHVCs. “Grown” halos, however, allowed clouds with circular velocities up to $v_c \simeq 35$ km s $^{-1}$ without forming stars, virtually closing the gap between model clouds and observed galaxies. The profiles which result from a gradually growing halo produce a significantly better match to the shape of the CDS, though the excess at low EW does, and should remain because the sub-halos are still there affecting the cloud cross section to absorption at low column density (though their effects cannot be modeled with a 1-D simulation).

I make the following conclusions:

1. N-body/hydro simulations fail to predict the observed void clouds; diffuse sheets cannot explain the absorbers.
2. The NFW halo must be rejected as an absorber model on a similar basis; it cannot explain the observed void clouds if “NFW” is taken to adequately represent the mass distribution *beyond* the virial radius.
3. A halo more massive than NFW is needed to explain observations. I find that a model consistent with a non-singular inverse square DM density profile, with a large truncation radius, is consistent with the data.

10. ACKNOWLEDGMENTS

I thank my advisor Hyron Spinrad for his encouragement and support during my stay at Berkeley. I am grateful to Christopher McKee for his incisive inspection of my work and for many useful suggestions. I wish to express my appreciation to the anonymous referee for helpful comments. My research was funded in part by NSF grant AST-0097163, and the Department of Astronomy at the University of California, Berkeley.

REFERENCES

- Arbabi-Bidgoli, S. & Müller, V. 2002, MNRAS, 332, 205
 Barkana, R. & Loeb, A. 1999, ApJ, 523, 54
 Bi, H. 1993, ApJ, 405, 479
 Blanton, M. R., and collaborators 2001, AJ, 121, 2358
 Blitz, L., Spergel, D. N., Teuben, P. J., Hartmann, D., & Burton, W. B. 1999, ApJ, 514, 818
 Braun, R. & Burton, W. B. 1999, A&A, 341, 437
 —. 2000, A&A, 354, 853
 Braun, R., De Heij, V., & Burton, W. B. 2002, American Astronomical Society Meeting, 200, 000
 Bullock, J. S., Kolatt, T. S., Sigad, Y., Somerville, R. S., Kravtsov, A. V., Klypin, A. A., Primack, J. R., & Dekel, A. 2001, MNRAS, 321, 559
 Carswell, R. F. & Rees, M. J. 1987, MNRAS, 224, 13P
 Cen, R. & Ostriker, J. P. 1999, ApJ, 514, 1
 Chernomordik, V. V. & Ozernoy, L. M. 1993, ApJ, 404, L5
 Croft, R. A. C., Weinberg, D. H., Katz, N., & Hernquist, L. 1998, ApJ, 495, 44
 Cruzen, S., Wehr, T., Weistrop, D., Angione, R. J., & Hoopes, C. 2002, AJ, 123, 142
 Davé, R. & Tripp, T. M. 2001, ApJ, 553, 528
 Davé, R., Hernquist, L., Katz, N., & Weinberg, D. H. 1999, ApJ, 511, 521

- de Heij, V., Braun, R., & Burton, W. B. 2002, A&A, 000
- Dey, A., Spinrad, H., & Dickinson, M. 1995, ApJ, 440, 515
- Dinshaw, N., Foltz, C. B., Impey, C. D., & Weymann, R. J. 1998, ApJ, 494, 567
- Dinshaw, N., Weymann, R. J., Impey, C. D., Foltz, C. B., Morris, S. L., & Ake, T. 1997, ApJ, 491, 45
- Djorgovski, S. G., Castro, S., Stern, D., & Mahabal, A. A. 2001, ApJ, 560, L5
- El-Ad, H. & Piran, T. 1997, ApJ, 491, 421
- . 2000, MNRAS, 313, 553
- Firmani, C., D'Onghia, E., Chincarini, G., Hernández, X., & Avila-Reese, V. 2001, MNRAS, 321, 713
- Grogin, N. A., Geller, M. J., & Huchra, J. P. 1998, ApJS, 119, 277
- Gunn, J. E. & Peterson, B. A. 1965, ApJ, 142, 1633
- Hernquist, L., Katz, N., Weinberg, D. H., & Jordi, M. 1996, ApJ, 457, L51
- Hoyle, F. & Vogeley, M. S. 2002, ApJ, 566, 641
- Huchra, J. P., Geller, M. J., & Corwin, H. G. 1995, ApJS, 99, 391
- Huchra, J. P., Geller, M. J., de Lapparent, V., & Corwin, H. G. 1990, ApJS, 72, 433
- Huchra, J. P., Vogeley, M. S., & Geller, M. J. 1999, ApJS, 121, 287
- Hui, L. & Gnedin, N. Y. 1997, MNRAS, 292, 27
- Katz, N., Weinberg, D. H., & Hernquist, L. 1996, ApJS, 105, 1+
- Klypin, A. 2002, Modern Cosmology, ed. S. Bonometto, V. Gorini, & U. M. (eds) (Bristol and Philadelphia)
- Klypin, A., Kravtsov, A. V., Valenzuela, O., & Prada, F. 1999, ApJ, 522, 82
- Manning, C. V. 2003 in *The IGM/Galaxy Connection: The Distribution of Baryons at $z = 0$* , eds. J. Rosenberg & M. Putman, (Germany: Kluwer Academic Publishers)
- Manning, C. V. 2002, ApJ, 574, 599 (Paper 1)
- Marzke, R. O., Huchra, J. P., & Geller, M. J. 1996, AJ, 112, 1803
- Mathis, H. & White, S. D. M. 2002, MNRAS, 337, 1193
- McKay, T. A., Sheldon, E. S., Johnston, D., Grebel, E. K., Prada, F., Rix, H., Bahcall, N. A., Brinkmann, J., Csabai, I., Fukugita, M., Lamb, D. Q., & York, D. G. 2002, ApJ, 571, L85
- McLin, K. M., Stocke, J. T., Weymann, R. J., Penton, S. V., & Shull, J. M. 2002, ApJ, 574, L115
- Miralda-Escudé, J., Cen, R., Ostriker, J. P., & Rauch, M. 1996, ApJ, 471, 582
- Morris, S. L., Weymann, R. J., Anderson, S. F., Hewett, P. C., Francis, P. J., Foltz, C. B., Chaffee, F. H., & MacAlpine, G. M. 1991, AJ, 102, 1627
- Morris, S. L., Weymann, R. J., Dressler, A., McCarthy, P. J., Smith, B. A., Terrile, R. J., Giovanelli, R., & Irwin, M. 1993, ApJ, 419, 524
- Navarro, J. F., Frenk, C. S., & White, S. D. M. 1996, ApJ, 462, 563
- Navarro, J. F., Frenk, C. S., & White, S. D. M. 1997, ApJ, 490, 493
- Osterbrock, D. 1989, *The Astrophysics of Gaseous Nebulae and Active Galactic Nuclei* (Mill Valley: Univ. Science Books)
- Penton, S. V., Shull, J. M., & Stocke, J. T. 2000b, ApJ, 544, 150
- Penton, S. V., Stocke, J. T., & Shull, J. M. 2000a, ApJS, 130, 121
- Pustil'nik, S., Ugryumov, A. V., Lipovetsky, V. A., Thuan, T. X., & Guseva, N. 1995, ApJ, 443, 499
- Rauch, M. 1998, ARA&A, 36, 267
- Rees, M. J. 1986, MNRAS, 218, 25P
- Richtmyer, R. & Morton, K. M. 1967, *Difference Methods for Initial-Value Problems* (New York: Interscience)
- Riediger, R., Petitjean, P., & Muckett, J. P. 1998, A&A, 329, 30
- Schechter, P. 1976, ApJ, 203, 297
- Seldner, M. & Peebles, P. J. E. 1977, ApJ, 215, 703
- Shull, J. M., Giroux, M. L., Penton, S. V., Tumlinson, J., Stocke, J. T., Jenkins, E. B., Moos, H. W., Oegerle, W. R., Savage, B. D., Sembach, K. R., York, D. G., Green, J. C., & Woodgate, B. E. 2000, ApJ, 538, L13
- Shull, J. M., Roberts, D., Giroux, M. L., Penton, S. V., & Fardal, M. A. 1999, AJ, 118, 1450
- Shull, J. M., Stocke, J. T., & Penton, S. 1996, AJ, 111, 72
- Sternberg, A., McKee, C. F., & Wolfire, M. G. 2002, ApJS, 143, 419
- Stocke, J. T., Shull, J. M., Penton, S., Donahue, M., & Carilli, C. 1995, ApJ, 451, 24
- Szomoru, A., van Gorkom, J. H., & Gregg, M. D. 1996a, AJ, 111, 2141
- Szomoru, A., van Gorkom, J. H., Gregg, M. D., & Strauss, M. A. 1996b, AJ, 111, 2150
- Thoul, A. A. & Weinberg, D. H. 1995, ApJ, 442, 480
- Tripp, T. M., Lu, L., & Savage, B. D. 1998, ApJ, 508, 200
- Tully, R. B. & Pierce, M. J. 2000, ApJ, 533, 744
- Wechsler, R. H., Bullock, J. S., Primack, J. R., Kravtsov, A. V., & Dekel, A. 2002, ApJ, 568, 52
- Weinberg, D. H., Hernquist, L., Katz, N., Croft, R., & Miralda-Escudé, J. 1997, in *Structure and Evolution of the Intergalactic Medium from QSO Absorption Line System*, 133
- Zabludoff, A. I. & Mulchaey, J. S. 2000, ApJ, 539, 136
- Zaritsky, D., Smith, R., Frenk, C., & White, S. D. M. 1997, ApJ, 478, 39
- Zaritsky, D. & White, S. D. M. 1994, ApJ, 435, 599
- Zheng, W., Kriss, G. A., Telfer, R. C., Grimes, J. P., & Davidsen, A. F. 1997, ApJ, 475, 469+